Fall 11-7-2019

Mechanical Characterization of Additively Manufactured Inconel 625 and AlSi10Mg via High-Throughput Tensile Testing

Aron Robbins

Aron S. Robbins

Candidate

Mechanical Engineering

Department

This thesis is approved, and it is acceptable in quality and form for publication:

Approved by the Thesis Committee:

Dr. Yu-Lin Shen, Chairperson

Dr. Tariq Khraishi, Professor

Dr. Jay Carroll, Senior Member of Technical Staff, SNL

Mechanical Characterization of Additively Manufactured Inconel 625 and AlSi10Mg via High-Throughput Tensile Testing

by

Aron S. Robbins

B.S. in Civil Engineering, University of New Mexico, 2017

THESIS

Submitted in Partial Fulfillment of the
Requirements for the Degree of

Master of Science

Mechanical Engineering

The University of New Mexico
Albuquerque, New Mexico

December, 2019

ACKNOWLEDGMENTS

I would like to acknowledge everyone who supported me with this study and throughout my master's degree. My friends and family made it possible to keep going even when things got tough. Dr. Jay Carroll for his invaluable guidance and mentoring during this project. Dr. Yu-Lin Shen for his direction and being the chair of my defense committee. Dr. Tariq Khraishi for joining my defense committee. Dr. Ben White, Sara Dickens, and Bonnie McKenzie for all their help with SEM/EDS analysis. Dr. Cole Yarrington, Dr. Thomas Ivanoff and Austin Baird for guidance and reviewing my paper. Dr. E.W. (Ted) Reutzel and Evan J. West of ARL Penn State for planning and coordinating these experiments and providing samples and related data. And finally, the entire Ductile Mechanics team for their assistance in my professional development.

This material is based in part on work performed by the Applied Research Laboratory at the Pennsylvania State University (ARL Penn State) supported by the NAVAL SEA SYSTEMS COMMAND (NAVSEA) under Contract No. N00024-12-D-6404, Task Order No. N0002417F8346.

Sandia National Laboratories is a multimission laboratory managed and operated by National Technology & Engineering Solutions of Sandia, LLC, a wholly owned subsidiary of Honeywell International Inc., for the U.S. Department of Energy's National Nuclear Security Administration under contract DE-NA0003525. SAND2019-12790 T

Mechanical Characterization of Additively Manufactured Inconel 625 and AlSi10Mg via High-Throughput Tensile Testing

by

Aron Robbins

B.S., Civil Engineering, University of New Mexico, 2017

M.S., Mechanical Engineering, University of New Mexico, 2019

Abstract

Additive manufacturing allows for the development of complex geometrical designs that may otherwise be impossible to fabricate through common methods. This advantage has opened the door to a new testing method capable of rapid and efficient material property characterization and qualification. The technique exhibits how 100's of sub-size tensile bars can be tested to show an inherent statistical variation of materials produced by laser powder bed fusion. The testing technique presented is used to evaluate various heat treatments of the nickel super-alloy Inconel 625 and the aluminum alloy AlSi10Mg after stress relief annealing. Statistical analysis using 3-parameter Weibull distributions is used to determine low-probably extreme values of both material's mechanical properties. Abnormally low ductility values of hot isostatic pressed Inconel 625 are determined to be due to the presence of large carbides along grain boundaries, characterized by electron dispersive spectroscopy (EDS). Incorrect processing parameters lead to the formation of lack of fusion voids in the Al-alloy, significantly reducing the effective load-bearing cross-sectional and triggering premature failure.

Table of Contents

List of Figures

List of Tables

Chapter 1 – Introduction

Additive manufacturing (AM) is a 3D printing process used for a variety of materials including polymers, ceramics, and metals **[1, 2]**. Fabrication of parts is completed layer-by-layer, allowing for complex designs that may be too costly or even impossible to manufacture with traditional manufacturing processes **[3]**. While the AM industry has been around for decades, interest in the methodologies has spiked in recent years as research continues to develop the industry **[4, 5]**. Most AM processes available today are powder or wire-based and utilize heating sources such as lasers, electron beams, and plasma arcs **[6]**. The process of interest in this study is the fabrication of metal components by laser powder bed fusion (LPBF) because of its wide application in industry. Two materials are characterized here; the nickel-superalloy Inconel 625 strengthened by the alloying elements Cr, Mo, and Nb, and the aluminum alloy AlSi10Mg. Inconel 625 has applications in the aerospace, aeronautical, chemical, and marine industries due to its excellent mechanical performance and resistance to high-temperature corrosion **[7]**. Aluminum-Silicon alloys are found in the automotive and aerospace industries due to their high strength-to-weight ratio and high thermal conductivity **[8]**. Both alloys under investigation are well known for their manufacturability via the LPBF AM process **[9, 10]**.

Section 1.1: Need for Study

While the AM process has gained popularity in recent years, it is still relatively young and has not been universally optimized. Numerous studies have determined ideal fabrication parameters **[7, 11, 12]**, however, these parameters are material specific and

often don't apply to other powder or printers from other vendors **[13]**. All parts produced by AM come with defects that can include porosity, cracking, warping, excessive surface roughness, residual stress, and limited dimensional accuracy **[14]**. Rapid heating and cooling during the AM process produces thermal gradients within printed parts, resulting in residual stresses once the build is complete. Subsequent heat treatments are typically required to reduce the amount of residual stress and alter the material to achieve desired mechanical properties. Effects of various heat treatments are well documented, but a significant amount of variation exists between presented results due to a limited quantity of components tested. A larger sample population is required to provide a range of expected material properties based on process parameters and ensuing heat treatments.

Precipitation kinetics of Inconel 625 is a popular topic of research and the phase transformation of the material produced by LPBF is attracting attention. Amato et al. observed precipitates rich in Nb along the melt pool boundaries in the as-built condition **[15]**. Li et al. also found nano-sized precipitates, perceived to be rich in Nb and Mo via EDS, within the matrix **[7]**. TEM analysis conducted by Keller did not identify precipitates in the as-built material **[16]**. After stress relief annealing, Lass et al. discovered precipitates with a plate-like morphology located in the interdendritic regions. These precipitates were identified as δ-phase by means of x-ray diffraction (XRD) and selected area electron diffraction (SAED) **[10]**. Solution annealing resulted in the formation of Cr oxides and Cr-rich precipitates, as determined by Li et al **[7]**. Keller found that after annealing at a temperature of 1150°C, M6C carbides and the Laves phase were the dominant precipitates **[16]**. The variation of observed precipitation and its effect on mechanical properties is a major focus of this study.

The aluminum alloy characterized in this study is known for its susceptibility to porosity during LPBF fabrication. Several forms are common, including lack of fusion, gas porosity, keyhole porosity, and pre-existing pores present in the powder feedstock. Lack of fusion pores are typically formed due to inclusions in the powder feedstock and process parameter errors such as hatch spacing, laser power, and scanning speed **[17]**. Gas porosity is common in the alloy because aluminum reacts with water to liberate hydrogen gas that is then injected into the melt pool, forming spherical pores **[9, 18]**. Keyhole porosity typically occurs due to the evaporation of liquid aluminum **[19]**. Lack of fusion is the dominant cause of porosity observed in this study, although some gas porosity is present.

Section 1.2: Focus of Study

This study introduces the use of a high-throughput tensile testing procedure that allows for the rapid characterization of mechanical performance of additively manufactured materials. Hundreds of sub-size tensile bars are tested, and the results are processed with the use of a series of MatLab™ scripts to reduce analysis time. An acceptance testing procedure is also presented that allows for build qualification without sacrificing significant space in the build tray.

It is necessary to understand the effects of various heat treatments on Inconel 625 mechanical properties, and correlation with the microstructure evolution and formation of precipitates provides better insight into the fabrication process. The mechanical performance exhibited by the varying heat treatments is linked to the microstructure and compared with the results presented in other studies. Differences between the properties

of the current material and those given in other reports are presented as a variation in the tensile specimen size and the surface roughness effects on the observed mechanical behaviors.

Porosity is common in AlSi10Mg and the material used in this study is no exception. The cause of substantial porosity present in the alloy is required to optimize process parameters. Relating the effects of porosity on density and effective load bearing area is needed to understand just how detrimental incorrect processing parameters can be. Understanding these relationships will help qualify AM components by assessing the quantitative impact of their flaws.

A statistical examination of low-probability extreme values is conducted with the use of 3-parameter Weibull distributions. The distributions are applied to the mechanical properties of the two materials in this study to understand worst-case scenarios. Low-probability extreme values are valuable qualities that are beneficial in terms of component design. AM components don't always meet specifications set in the standards (e.g. ASTM, ISO, ANSI, etc.), so designing for these values provides a level of safety.

The following chapters present an in-depth look at the materials and methods used in the study. Chapter 2 introduces the high-throughput testing procedure and material characterization. The mechanical properties of Inconel 625 and the variation between heat treatments, along with statistical analysis and correlation to microstructure, are given in Chapter 3. Chapter 4 presents the effects of porosity on results from an acceptance testing procedure as well as the high-throughput mechanical properties. Finally, Chapter 5 summarizes the findings presented in this thesis.

Chapter 2 – Experimental Materials and Methods

Two additively manufactured materials, a nickel super-alloy, Inconel 625 (IN625), and an aluminum alloy, AlSi10Mg, are presented and analyzed in this thesis. Both materials are fabricated using a laser powder bed fusion process (LPBF) that involves melting layers of powder to form a part in an inert gaseous environment. As shown in Figure 1, a layer of powder is moved from the powder supply to the build tray via a roller with layer thicknesses in the micron range, and a laser beam melts an area according to the CAD design. After the sintering is complete, the build tray moves down, and a new layer of powder is rolled on top of the previous layer. This process continues until the part is completely printed. This chapter will introduce a unique specimen design fabricated by the LPBF process, as well as material characterization of the aluminum and nickel alloys, and finally an unparalleled testing procedure used for rapid characterization of mechanical properties.

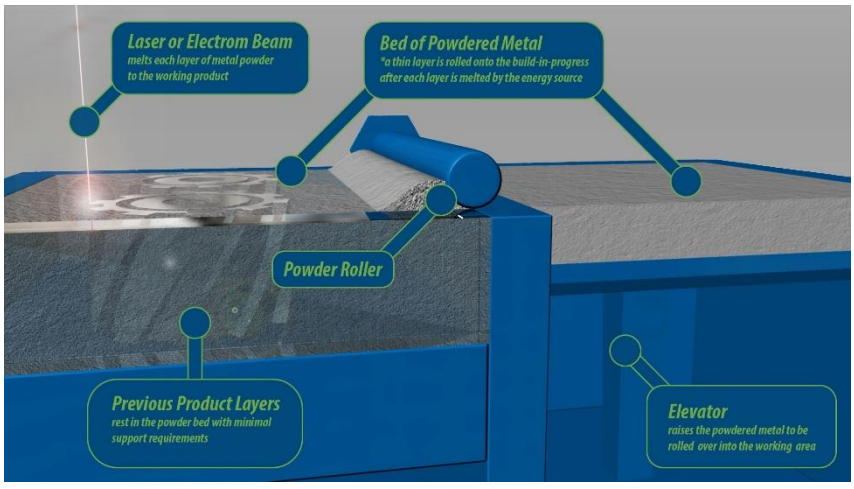

Figure 1: Laser powder bed fusion schematic

Source: https://www.3diligent.com/3d-printing-service/powder-bed-fusion/

Section 2.1: Specimen Design and Mechanical Testing

In order to address the limitations of additive manufacturing, as well as expedite the testing procedure, a custom size tensile bar designed by Boyce and Salzbrenner **[13, 20]** is used. The nominal geometry of the samples incorporated a 1 mm by 1 mm cross-section and a 4 mm gauge length. Although the tensile bars do not meet ASTM geometry standards **[21]**, the gauge length meets the 4-to-1 ratio to the cross-section to ensure comparable elongation results to standard size samples. The 45° slope of the grip heads were designed to eliminate the horizontal overhang limitations of the additive manufacturing process and allow for rapid alignment in the high-throughput testing procedure **[22]**. Tensile bars are aligned on a support rack with 1 mm spacing between them and printed together as one piece to significantly reduce the need for operator intervention, as shown in Figure 2. The AlSi10Mg samples were printed with 40 bars per rack while the IN625 samples were printed with 25 bars per rack, with the system designed for up to 50 bars spaced 1 mm apart. Each rack of specimens is printed with the tensile axis parallel to the build direction.

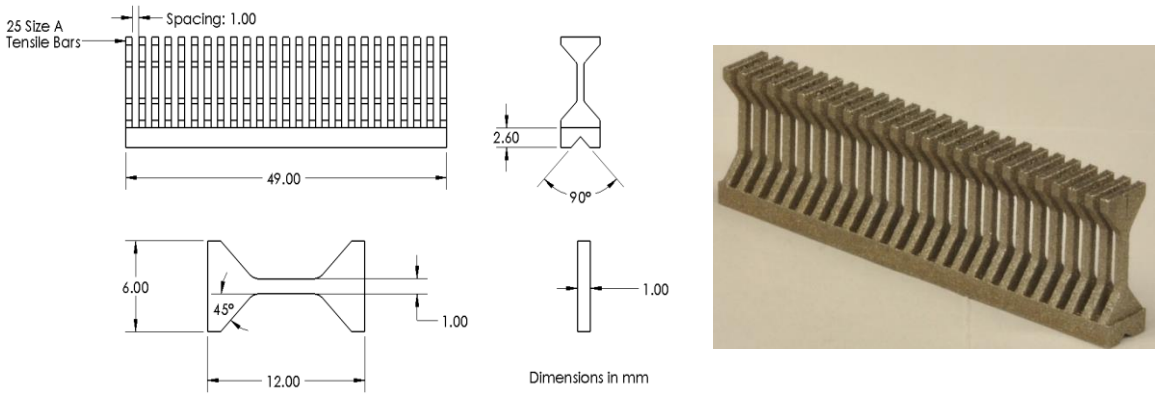

Figure 2: Tensile specimen geometry

Shown in Figure 3 is an image containing the major components used in high-throughput testing: cameras for DIC and area measurements (a) and (b), (c) a reference standard for pixel-to-mm ratio (c), a screw-driven linear stage with motion control (d), self-aligning tensile grips (e), and most importantly the tensile racks (f). The self-aligning

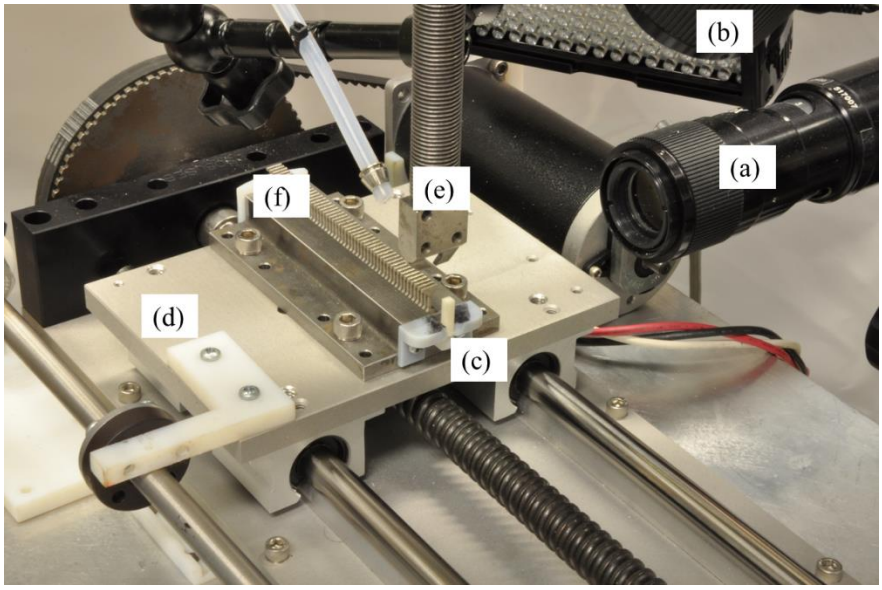

Figure 3: a), b) Cameras used for DIC and area measurements, c) reference standard, d) screw driven linear stage with motion control, e) self-aligning grips, f) tensile rack

grips are attached to an Interface 2000 lbf (8900 N) load cell on an MTS servo-hydraulic load frame. Automation and high throughput are synonymous when it comes to testing, and to reduce the need for operator intervention, live strain tracking using VIC-Gauge™ software by Correlated Solutions is implemented in the procedure. Further automation includes non-contact cross-sectional area measurements with the use of two cameras, viewing the front and side faces, and the use of a reference standard to provide a pixel-to-mm ratio for post-process image analysis. The testing procedure includes a 2% strain unload to 50 N and then reloading again to failure to provide a more accurate Young's modulus determination. The modulus unload loop corrects for machine compliance and

any misalignment that may be present. Due to the naturally low ductility of AlSi10Mg, the modulus unload loop started at 0.5% strain and unloaded to 25 N to ensure enough data points were recorded prior to failure.

Previous studies using an earlier rendition of this testing procedure **[13]** were able to accurately track strain without the use of a speckle pattern due to the inherent rough texture of additively manufactured specimens. In the current testing procedure, the use of additional lighting introduces shadowing effects on the face of the samples as they are pulled in tension, altering the accuracy of the strain tracking measurements. A white base coat and black speckle pattern are applied to achieve desirable patterns, as governed by **[23]**. The displacement rate for all tests is 0.05 mm/sec resulting in a gauge strain rate of $\sim 1 \times 10^{-2}$ s^{-1}. Subset size has proven to be an important factor in the accuracy of DIC **[24]**, and work using the existing system **[13]** has shown that a subset size of about half of the gauge width results in a good compromise between accurate strain tracking and noise in the strain signal. Strain tracking is acquired at 30 Hz throughout each test, however, images are taken at a rate of 2 Hz to allow for full-field DIC analysis, resulting in ~50 GB of data per 50 tensile bars pulled. The live strain tracking significantly reduces the amount processing time, as applying a scalar to the voltage acquired during testing produces strain measurement throughout the entire test. One image from each camera, taken prior to loading each sample, is required to estimate the cross-sectional area. The images are then processed using the MatLab™ software package AVID: Area Values from Image Dimensions ©. The first image of every test is of a reference standard of known dimensions, setting the pixel-to-mm ratio for the rest of the images. The first front and side images of each sample are then selected, and a first-degree polynomial line is fit

to either edge of the specimen, as shown in Figure 4. The distance between lines is measured by the difference in the pixel location of the line along the x-axis. Measurements are taken at every y-axis pixel that the two lines are fit to, and the average of these values is used as the width dimension in pixels. The mm-to-pixel ratio is applied to produce width measurements of either face in millimeters. Area measurements are then inputted to the MatLab package BATS: Batch Analysis of Tensile Specimens ©, that produces yield stress and strain at a 0.2% offset, elastic modulus, ultimate tensile strength, uniform elongation, and elongation at failure. The yield strain, uniform elongation, and elongation to failure are determined by applying a percent strain per volt (%strain/volt) scalar to the voltage output by VIC-Gauge. Area measurements for each individual tensile bar are applied to normalize the force values into stress measurements and are output in units of MPa. Elongation at failure measurements are made by applying a scalar to the stress values for each sample. Once the actual stress values fall below the scaled stresses after the stress has peaked (UTS), the strain at that value is used as the ductility. For the tests presented in this thesis, a scalar of 0.5 is used.

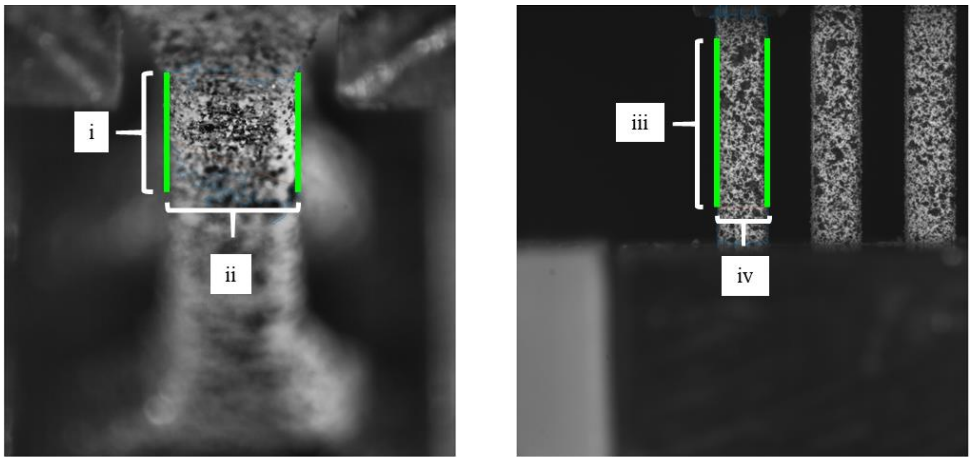

Figure 4: (a) front and (b) side line fits

The front-facing camera is positioned above the tensile racks and viewing down at a 45° angle so that the image isn't obscured by the previous sample. The adjusted field of view creates a limited range of view for the specimen, however, the 4.1 MPx Point Grey camera and 12 mm Navitar™ lens attachment, SN 1-50504, provide sufficient depth of field and a high-quality image. The line fit (i) in Figure 4 (a) represents approximately 500 pixels. Pixel measurements between the lines fit to the reference standard reveal a coefficient of variation of less than 1% from the top to the bottom of the standard, suggesting the trapezoidal view of the image introduces minimal error to the width approximations.

The efficiency of high-throughput testing doesn't come without drawbacks. While the strain tracking has been optimized, the accuracy of area measurements is limited. The size and spacing of the tensile racks, the natural surface roughness of additively manufactured parts, and the high-throughput connotation all make individual contact measurements antiquated at best. A support rack was created that allowed for individually printed sub-size tensile bars to be tested in the high-throughput system. Cross-sections of a set of bars were calculated via micrometer measurements and compared to those output by the AVID image processing code. An average measurement error of 3% ± 2% (standard deviation) was found and the areas that were manually measured were all less than those measured digitally. The over-estimation in the cross-sectional area provided by the AVID measurements reports conservative strength values. As mentioned earlier in the chapter, the effect of surface roughness on cross-sectional area measurements will be discussed as the mechanical properties of each material are presented.

Speed and automation are equally relevant in terms of high-throughput testing, and the procedure presented here significantly reduces testing time and the need for operator intervention. Ductile samples, >30% elongation at failure, require ~1 hour of time to test 50 samples. Less ductile samples, such as the aluminum alloy studied in this thesis, require less time to complete testing. A basic analysis of the data, using the AVID and BATS MatLab software packages, can present raw results in 20 minutes with minimal errors. These two procedures combined allow for rapid characterization of mechanical properties and in a typical day, ~400 samples, along with the results, can be processed.

Section 2.2: Density, Hardness, and Charpy Impact Toughness

Destructive testing of components that have been additively manufactured is not always feasible, so other methods of qualifying the printed material properties are necessary. An acceptance testing procedure has been developed as a means of accurately and consistently predicting material performance without destroying the actual components. Charpy impact specimens, printed on the build plate in addition to the components, act as an excellent test article that can be used to measure density, hardness, and energy absorption without sacrificing a significant amount of real-estate on the build tray. The density of materials fabricated through the powder bed additive manufacturing process are greatly affected by process parameters, and there is a strong relationship between density and porosity of the printed parts. An increase in porosity has shown to have a negative effect on ductility and fracture toughness, thus justifying the use of density measurements and their ability to provide a quality metric for build property

verification **[9, 17, 25]**. Hardness and impact toughness measurements provide further verification as a comparison metric between builds and with the cast and wrought materials. The Rockwell hardness tests can be empirically related to tensile strength and ductility, among other physical characteristics, and require minimal time to obtain results **[26]**. Charpy impact toughness measurements are not easily related to conventional fracture toughness, but they do provide good measurements of a material's ability to withstand fracture, especially in brittle materials **[27]**.

As received Charpy bars are cut to length in accordance with ASTM E23 **[28]** and the top of each bar, in relation to the build direction, is marked and used as a reference for consistency. Two faces of the specimen are then polished via sandpaper to reduce inherent surface roughness, as uneven surfaces present inconsistency in hardness measurements. Once polished and cleaned, cross-sectional areas are measured, and the samples are used for density measurements via Archimedes' method **[29]**. Measurements are made using a Mettler Toledo balance fully equipped with a density kit, providing weight measurements with an accuracy of 0.1% or better. The technique used here employs the use of a polished steel ball of known density to determine the density of the water. Once the density of the water is calculated, and prior to the submerged weight measurement, the samples are placed under water and jostled to remove any trapped air bubbles. The proper wetting of the sample surface and removal of the air bubbles is imperative for accurate density calculations. The density of the Charpy samples are measured multiple times to account for variability and determine the accuracy of results based on the error bars. Hardness measurements are made following the Rockwell B (HRB) guidelines **[26]** with a 1/16" in diameter diamond ball applied at 100 kgf. Indents

are made with the two polished faces oriented as the resting surface and the surface to be indented. A quick study showed that by polishing the rest face and indent face, the hardness values increased 8% and the variability dropped from 6% to 1%. For each sample, a minimum of 4 hardness indentations are made, two on either end of the sample and far from the center of the bar or any edges, to limit the effect on the impact toughness and account for the discrepancy. Measurements at either end of the bar better represent the sample as a whole. After hardness measurements, the Charpy samples are v-notched and impact tested in accordance with ASTM standards **[28]**.

Section 2.3: Inconel 625 Characterization

The nickel alloy used in this study, Inconel 625 (IN625), is in part based on work with the Applied Research Laboratory at the Pennsylvania State University, supported by the NAVAL SEA SYSTEMS COMMAND. The process parameters for the IN625 used in this study are well documented by the manufacturer and are included in this section.

Composition	Units	ASTM F3056	Build 1 (virgin)	Build 2 (virgin)	Build 3 (reuse)
Al	Wt %	0.4 max	0.16	0.16	0.15
B	Wt %	-	<0.0005	<0.0005	<0.0005
C	Wt %	0.10 max	0.035	0.034	0.036
Co	Wt %	1.00 max	0.215	0.21	0.205
Cr	Wt %	20.00-23.00	21.39	21.22	21.23
Fe	Wt %	5.00 max	0.044	0.39	0.063
Mn	Wt %	0.50 max	0.0061	0.0064	0.0076
Mo	Wt %	8.00-10.00	8.81	8.68	8.75
Nb	Wt %	3.15-4.15	3.67	3.62	3.67
Ni	Wt %	Bal	65.3	65.8	65.6
P	Wt %	0.015 max	0.004	0.004	0.003
S	Wt %	0.015 max	0.0013	0.0012	0.0011
Si	Wt %	0.50 max	0.043	0.044	0.049
Ta	Wt %	-	<0.002	<0.002	<0.002
Ti	Wt %	0.40 max	0.12	0.12	0.13
O	Wt %	-	0.012	0.01	0.007
N	Wt %	-	0.006	0.006	0.007
H	Wt %	-	0.0007	0.0007	0.0009

Table 1: IN625 chemical composition

The powder used to fabricate the samples came from a single lot of Oerlikon's LaserForm Ni625 Type A powder and was supplied with the chemical analysis shown in Table 1. There is a slight variation in the powder chemistry between the two virgin builds as well as the reused powder, however, the differences are minuscule, and all three builds met the listed ASTM specifications.

A 3D Systems ProX 320 machine was used with an argon atmosphere set to 5.3 ± 0.3 bars. All three builds used in this study used a layer thickness of 60μm, a constant recoater speed of 115mm/sec, and OEM-recommended settings for laser power and scanning speed. Build 3 was printed with residual powder from builds 1 and 2 to qualify the difference in properties after recycling powder. Upon post-print inspection, it was found that the argon pressure and oxygen levels for builds 1 and 2 were abnormally high. The maximum pressures were 84 mbar and 93 mbar, with corresponding oxygen levels of 8 ppm and 4.5 ppm for builds 1 and 2, respectively. The cause of the discrepancy was determined to be a clogged filter in the machine. The equipment was cleaned prior to build 3, with environmental pressure measured at a maximum of 36 mbar and an upper oxygen level of 2.8 ppm for the third and final build. An increase in powder oxidization due to the increase in oxygen levels during printing may have an influence on the microstructure, mechanical properties, and porosity **[7, 30]**. While the oxygen's effect on observed results is briefly covered in the IN625 results chapter, a comprehensive investigation is necessary to better understand the impact oxygen levels play during the additive manufacturing of IN625.

In addition to tracking process parameters, the build layout was varied for all three builds in order to analyze the variability with respect to build location. Samples in

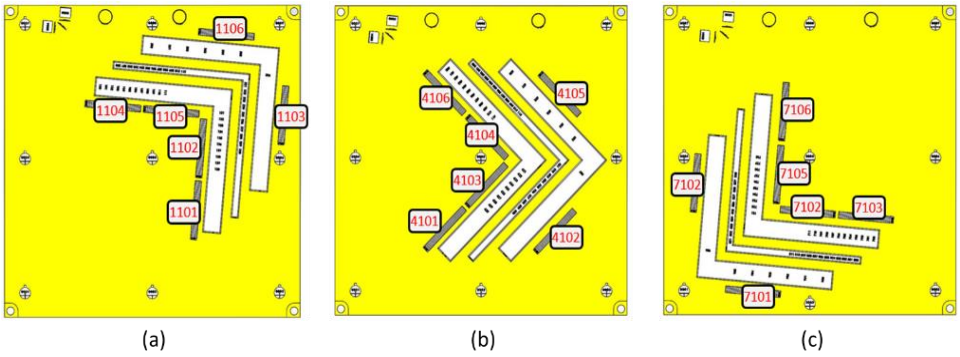

Figure 5: (a) Build layout 1, (b) build layout 2, (c) build layout 3

builds 1 and 3 were oriented parallel and perpendicular to the recoater blade and gas flow, depending on the specimen, while build 2 was oriented at a 45° angle to the silicon recoater blade. The build orientation with corresponding sample numbers is shown in Figure 5. Additional specimens were included in the build plate, but only the sub-size tensile bars are investigated in this study.

Heat treatments are used to adjust material properties and achieve more desirable traits, but due to the high amount of residual stress present in additively manufactured components, it is necessary to subject parts to a stress relief regime prior to treatment **[31, 32]**. After printing and initial inspection, each build plate was stress relieved (SR) with all constituents still attached. Following the stress relief heat treatment, the individual specimens were removed from the plate via wire electrical discharge machining (EDM). Selected samples from build plates 1 and 2 were then subjected to either a solution heat treatment (Sol HT) or hot isostatic press (HIP) conditioning. Due to time constraints the powder reuse specimens, referred to as build 3, were only subjected to stress relief heat treatment. The heat treatment schedule along with the guiding standard are listed in Table 2. All heat treatments were conducted at Bodycote Heat Treatments Ltd.

Heat Treatment	Schedule	Standard
Stress Relief	1040°C ± 15°C x 60 min ± 6 min	AMS 2774 E
Solution HT	1175°C ± 15°C x 60 min ± 6 min	AMS 2774 E
HIP	100 MPa 1120°C to 1175°C ± 15°F x 240 min ± 60 min and cool to under 425°C	ASTM F3301

Table 2: IN625 heat treatment schedule

Surface roughness is inherent in any additively manufactured part without any post-process correction and plays a much larger role in sub-size samples, discussed in greater detail in subsequent chapters. The surface roughness of the tensile racks was measured using a Bruker Contour GT-I optical interferometer. A 1 mm scan length magnified at 50x with a 50 µm backscan and 150 µm length setting along was used along with the rack support at the base of the tensile bars for roughness determination. The average roughness is calculated as the arithmetic mean of the absolute values of the profile heights over the entire scan length. The peak roughness is measured as the distance between the maximum profile height and the average roughness. It was noted by the manufacturer that the larger specimen coupons attached to build plates 1 and 2 show significantly more surface roughness than those of build 3, however, roughness measurements of the sub-size tensile bar racks did not reveal the same results. The

Sample	Ra (µm)	Rp (µm)
SR - Virgin	7.79	50.44
SR - Reuse	8.42	73
Sol. HT	7.65	64.59
HIP	8.52	51.89

Table 3: IN625 average surface roughness

increase in roughness observed on the upper portions of the large flat faces may be a result of the increase in oxygen levels and pressure in the chamber, however, studies have shown that an increase in oxygen levels do not negatively affect the material composition **[33]**. Two specimens from each heat treatment were selected for measurement as well as one specimen from the powder reuse build plate. The average and peak roughness values are given in Table 3.

The various heat treatments play a significant role in mechanical property variation, and the effect of heat treatment on the microstructure was studied after mechanical testing. Because the microstructure was analyzed post-testing, it is important that the area to be polished and viewed does not represent yielded material or the specimen's edges. For completeness and accuracy, the samples used for imaging were cut to an appropriate length near the bottom of a tensile grip using a diamond cut off wheel with an approximate grit of 50 μm. Samples were then polished using a Leica EM TXP at sandpaper grits of 9 μm, 2 μm, and finally 0.5 μm. Electron backscatter diffraction (EBSD) images are negatively affected by plastic strain on the imaging surface **[34]**, and in order to mitigate any deformation that may have occurred during mechanical polishing, the samples were ion polished in a Leica EM RES102 ion mill for 3 hours at a 5° milling angle. A Zeiss Supra 55-VP SEM was used for electron backscatter diffusion (EBSD) microstructural characterization and the same nominal location was selected on each sample to better represent the difference between heat treatments. Figure 6 shows both stress relieved specimens revealed columnar grain growth in the build direction. The melt pool geometry is evident in both stress relieved samples, and smaller equiaxed grains are observed at the edges of the melt pool. Both the HIP and Sol HT samples

recrystallized and coarsened into a more equiaxed grain structure, eliminating the columnar growth in the build direction. The formation of annealing twins are also present in the HIP and Sol. HT samples, as is common with low stacking-fault free energy FCC metals, due to the grain growth and recrystallization during the additional heat treatments **[35]**. Mosaicity, or microtexture within individual grains, is evident in the larger grains of all four samples imaged. Included in Figure 6 are inverse pole figures (IPF) that represent the grain orientation based on the EBSD map. The IPF maps are generated using half widths of 10° and cluster sizes of 5° and are presented on the same density scale to highlight differences between samples. The stress relieved samples display some texture in the <001> orientation, as observed in the elongated grains. The solution heat treated sample reveals a texture in the <101> and <111> directions, with orientations spread throughout the lower portion of the IPF. The HIPed sample reveals a <111> texture and a cluster around <304>. The role that the grain orientation plays on mechanical properties is discussed in detail in the IN625 results chapter.

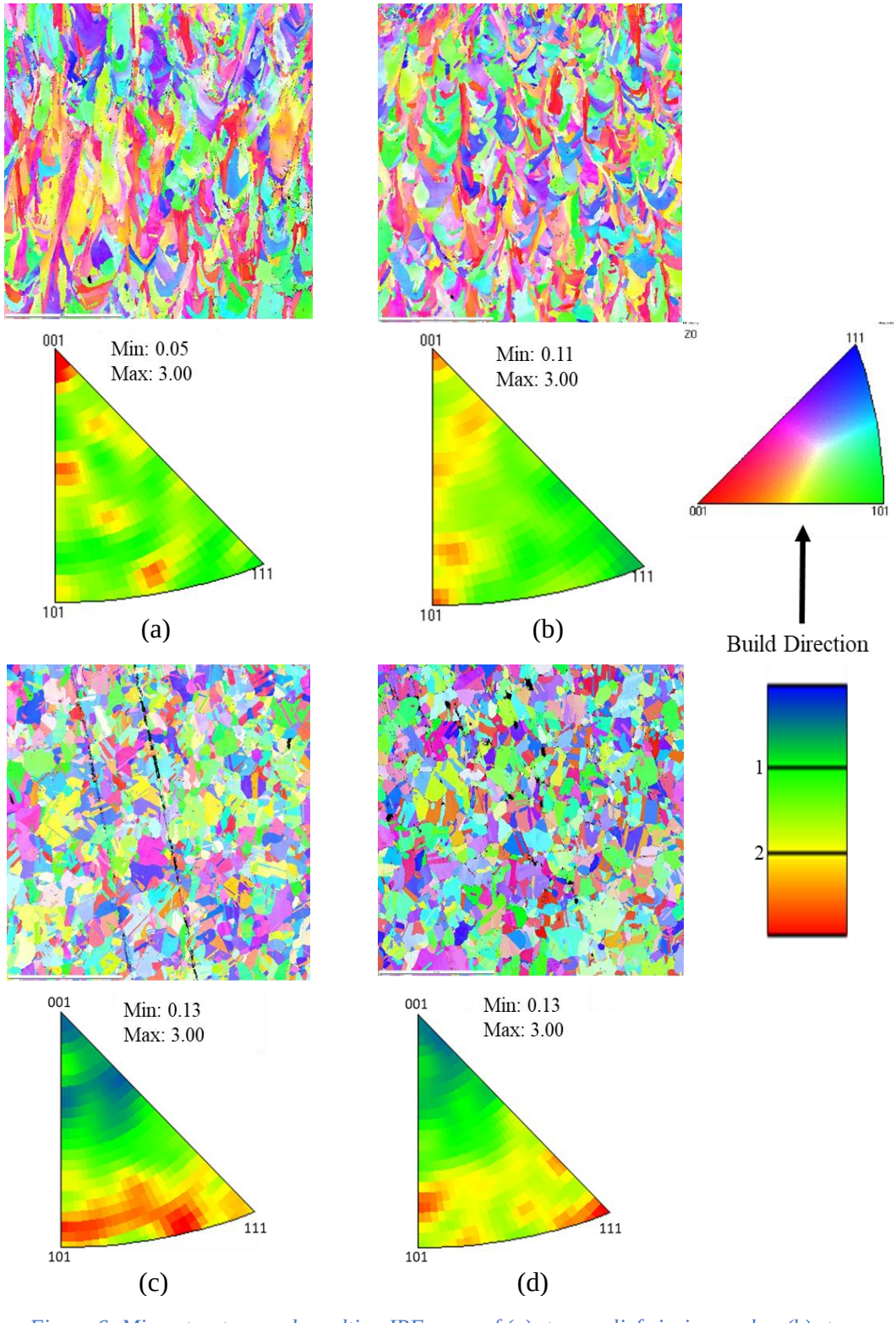

Figure 6: Microstructure and resulting IPF maps of (a) stress relief virgin powder, (b) stress relief reuse powder, (c) solution heat treat, (d) hot isostatic press heat treatments

The MTEX toolbox, a MatLab toolbox used for SEM/EBSD analysis, was used to determine the grain boundary misorientation. The grain growth in the build direction observed in the stress relieved samples reveal significantly lower grain boundary misorientation angles between boundaries when compared to the additional heat treatments, however, the angles are too large to be considered low angle boundaries **[36]**. The additional heat treatments resulted in a more equiaxed grain structure with higher grain boundary misorientation angles, with a majority in the range of 60°-70°. The increase in misorientation angles is due to the presence of annealing twins, representing a low stacking-fault free energy **[37]**. The grain boundary misorientation angle for each heat treatment is shown in Figure 7.

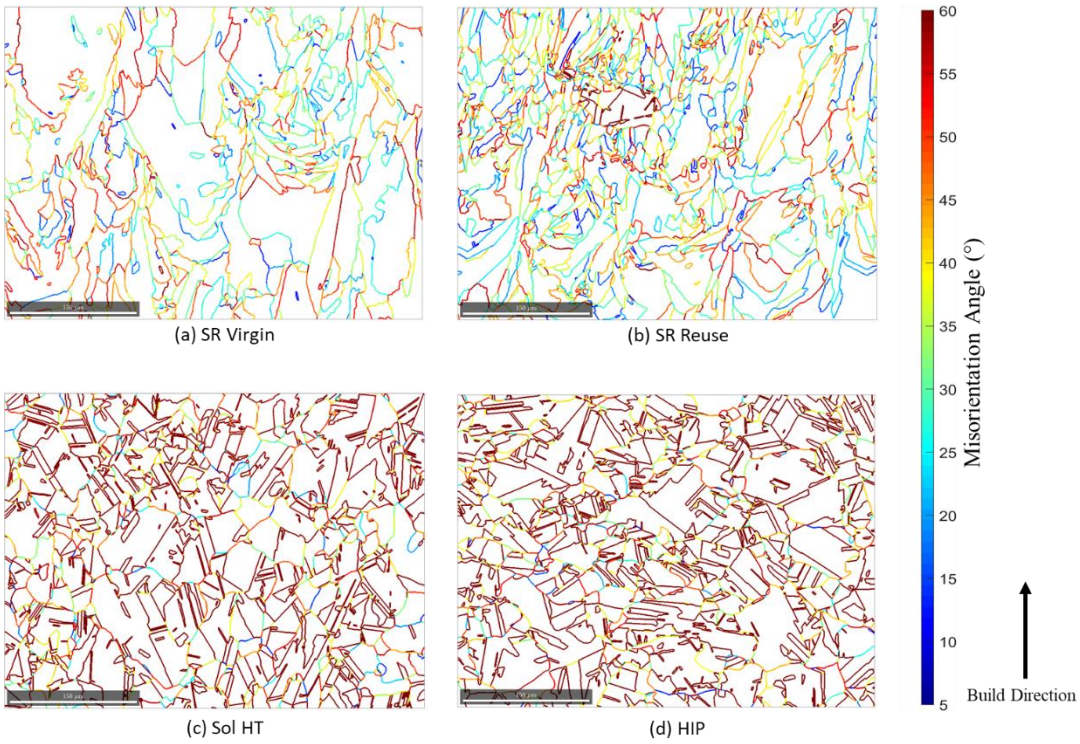

Figure 7: Grain boundary misorientation of (a) stress relief virgin powder, (b) stress relief reuse powder, (c) solution heat treat, (d) hot isostatic press

Section 2.4: AlSi10Mg Characterization

The aluminum alloy AlSi10Mg used in the study was supplied by CalRAM (California, USA) as part of a build qualification. The powder certification used in manufacturing the AlSi10Mg was provided by Valimet, Inc. (California, USA) and is listed in Table 4. The manufacturer's specification differed slightly from ASTM standards, namely in the allowable copper and iron specification, however, the as-received values were within tolerance. The ASTM and manufacturer's specifications are included in the table to show that the powder met the minimum requirements prior to printing.

Composition	Units	ASTM F3318	AM 103C Spec	As Received
Al	Wt %	Bal	Bal	Bal
C	Wt %	0.05 max	0.05 max	-
Ca	Wt %	0.05 max	0.05 max	-
Cr	Wt %	0.05 max	0.05 max	-
Cu	Wt %	0.05 max	0.03 max	<0.01
Fe	Wt %	0.55 max	0.40 max	0.07
Li	Wt %	0.05 max	0.05 max	-
Mg	Wt %	0.20-0.45	0.25-0.45	0.3
Mn	Wt %	0.45 max	0.15 max	0.01
N	Wt %	0.05 max	0.05 max	-
Ni	Wt %	0.05 max	0.05 max	<0.01
Pb	Wt %	0.05 max	0.05 max	<0.01
S	Wt %	0.05 max	0.05 max	-
Si	Wt %	9.0-11.0	9.0-11.0	9.78
Sn	Wt %	0.05 max	0.05 max	<0.01
Ti	Wt %	0.15 max	0.15 max	0.01
V	Wt %	0.05 max	0.05 max	-
Zn	Wt %	0.10 max	0.10 max	<0.01

Table 4: AlSi10Mg chemical composition

Two separate builds were used, each containing two racks of 40 tensile bars and printed using powder from the same lot. After printing was complete, the specimens remained on the build plate and were sent to EAS Manufacturing Co., Inc. (California, USA) for post-process heat treatment. The samples were stress relieved at 550°F ± 25°F

for 2 hours ± 15 minutes and air-cooled in accordance with AMS 2771. Upon receiving the samples, surface roughness measurements were conducted following the same procedure presented in the previous section. Listed in Table 5 are the average roughness values, R_a, and the peak roughness values, R_p, for the two racks from each build.

Sample	R_a (µm)	R_p (µm)
Build 1 R1	5.96	36.83
Build 1 R2	9.35	41.76
Build 2 R1	7.37	37.85
Build 2 R2	10.81	45.24

Table 5: AlSi10Mg surface roughness

Chapter 3 – Inconel 625 Super Alloy Results

This chapter presents the mechanical properties of the nickel alloy Inconel 625 (IN625) introduced in Chapter 2, along with the statistically determined lower limits of these properties. The role of the varying heat treatments effect on microstructure and resulting tensile properties is also brought into focus, as well as an analysis of the build location and reuse of printing powder. The chapter is concluded with an analysis of the sub-size tensile effect and characterization of the tensile bar fracture surfaces.

Section 3.1: Mechanical Properties

All IN625 tensile bars were printed in racks of 25 and tested using the high-throughput testing procedure described in Chapter 2. Figure 8 shows the engineering stress-strain curves for all ~450 tensile tests, grouped by heat treatment and powder

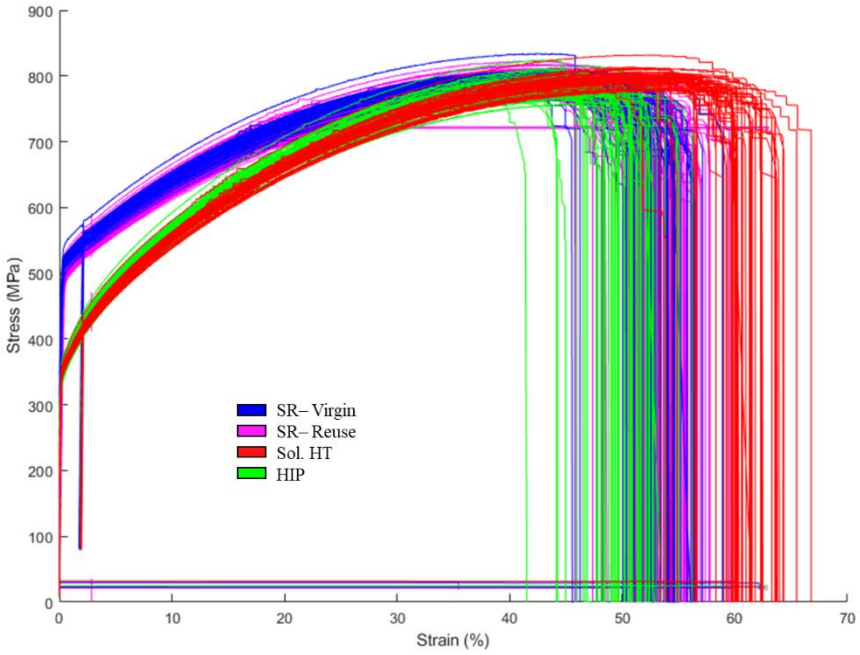

Figure 8: IN625 Stress-strain curves

condition. Both stress relieved powder states, virgin and once reused, reveal nominally identical mechanical properties, and the apparent variation seen in the reused powder samples is likely due to the increase in the sample population, as listed in Table 6.

Sample	No. of Specimens	Area (mm^2)	Modulus (GPa)	Yield Strength (MPa)	Ult. Tensile Strength (MPa)	Elongation at Failure (%)
SR – Virgin	93	1.17	141 ± 7	518 ± 9	792 ± 12	52 ± 3
SR - Reuse	149	1.16	141 ± 9	506 ± 10	790 ± 13	53 ± 2
Sol HT	99	1.16	171 ± 9	361 ± 6	798 ± 12	61 ± 3
HIP	94	1.18	174 ± 12	356 ± 7	782 ± 13	51 ± 3

Table 6: IN625 average mechanical properties

The stress relieved samples exhibited superior yield strength, about 512 MPa on average, when compared to the solution heat treated and HIPed values of 360 and 356 MPa, respectively. The significant decrease in yield stress can be attributed to an increase in grain size due to aging, as an increase in grain size is known to reduce yield strength through the Hall-Petch relationship **[38]**. The ultimate tensile strength values for all heat treatments fall within 1 standard deviation of the stress relieved samples, however, there is a 16 MPa difference between the Sol HT and HIP, with Sol HT having higher ultimate strength. The elastic modulus, calculated from the 2% strain unload loop mentioned in Chapter 2, showed the SR samples having the lowest modulus at 141 GPa, followed by the Sol. HT samples at 170 GPa, and the maximum modulus values are seen by the HIP specimens at 174 GPa. The variation in modulus values is anticipated to be invoked by the microstructure and preferred grain orientation and will be discussed in more detail later in the chapter. The elongation at failure was consistent for both stress relieved powder conditions, with values around 53% for all samples. The maximum ductility

values are produced by the Sol. HT samples at 61% elongation, while the HIP samples displayed the lowest values at 51%. The low ductility values produced by the HIP samples are inconsistent with expected mechanical properties, as the HIPing process is known to increase ductility at the expense of strength **[9, 13, 15, 37]**. Two routes were taken to better understand the lower-than-expected ductility: density measurements and SEM imaging with EDS analysis. The density measurements are used to determine the presence of voids or surface cracks, and SEM/EDS imaging is utilized for the characterization of precipitates and carbides that may exist. The SEM/EDS results are given later in the chapter and density is discussed next.

Two sets of tensile racks from each heat treatment specification were used to measure density, as calculated by Archimedes' principle mentioned in Chapter 2 **[29]**. Table 7 shows the measured density and percent dense relative to the elemental density of 8.61 g cm^3. The elemental density was calculated using the ratio of the weight percent to the density of each composing element. The higher density found in this study, relative to the published value of 8.44 g/cm^3 **[39]**, is linked to a higher weight percent of nickel. The pressure used in the HIP process has proven to reduce the number of pores and voids that are naturally present in additively manufactured components and increase relative density **[9, 13, 15, 37]**, however, the results found in this study suggest otherwise.

Sample	**Density (g/cm^3)**	**% Dense**
SR – Virgin	8.444	98.1 %
SR – Reuse	8.463	98.3 %
Sol. HT	8.460	98.3 %
HIP	8.427	97.9 %

Table 7: IN625 measured and relative density

While the exact determination is outside the scope of this study, two possibilities are presented as potential sources. Firstly, it is hypothesized that cracks on the surface of the sample, exaggerated by the HIPing process **[40]**, may have trapped air bubbles during the submerged weight measurement. Air bubbles present in the Archimedes' density determination will alter the accuracy of the measurement, resulting in lower density values. Computed tomography (CT) scans were conducted using a Zeiss Xradia Versa 520 with a voxel resolution of 3 μm to discover if surface cracks were present in the material. Due to a limited time frame, only one sample from the Sol HT and HIPed lots were imaged. The resulting scans, however, display crevices on the surface of the HIPed sample that propagate inwards. CT scans of the Sol HT show no signs on surface cracks, as displayed in Figure 9. Figure 10 shows CT images of the HIPed sample, displaying obvious inward crack propagation on the surface of the sample. The external voids shown provide evidence that air pockets may have been present during density measurements. Imaging of more HIPed samples, as well as the other heat treatments, is required to concretely determine if this is the cause of the abnormal measurements.

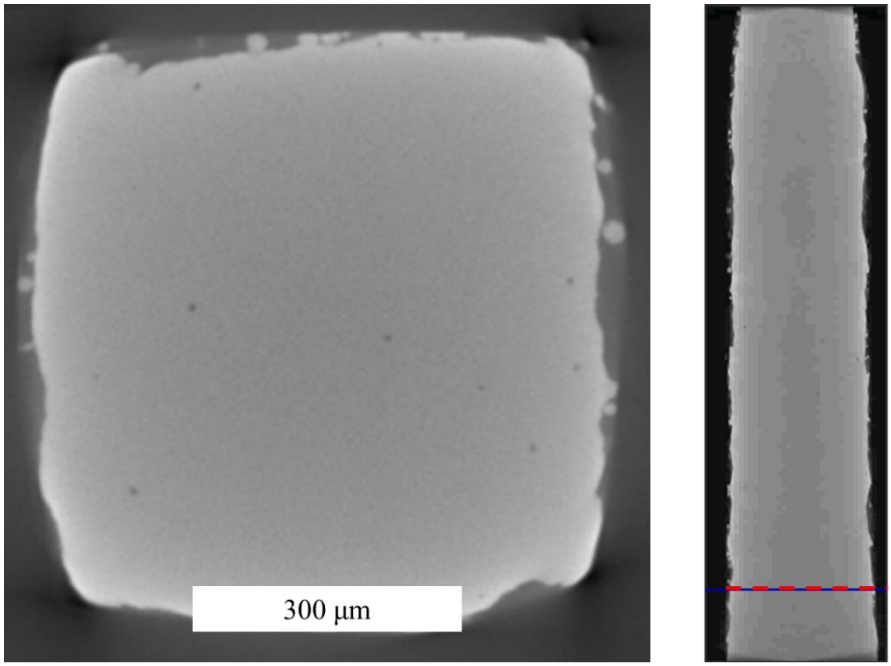

Figure 9: CT images of a solution treated sample showing (a) a view normal to the build direction, (b) plane location on tensile bar

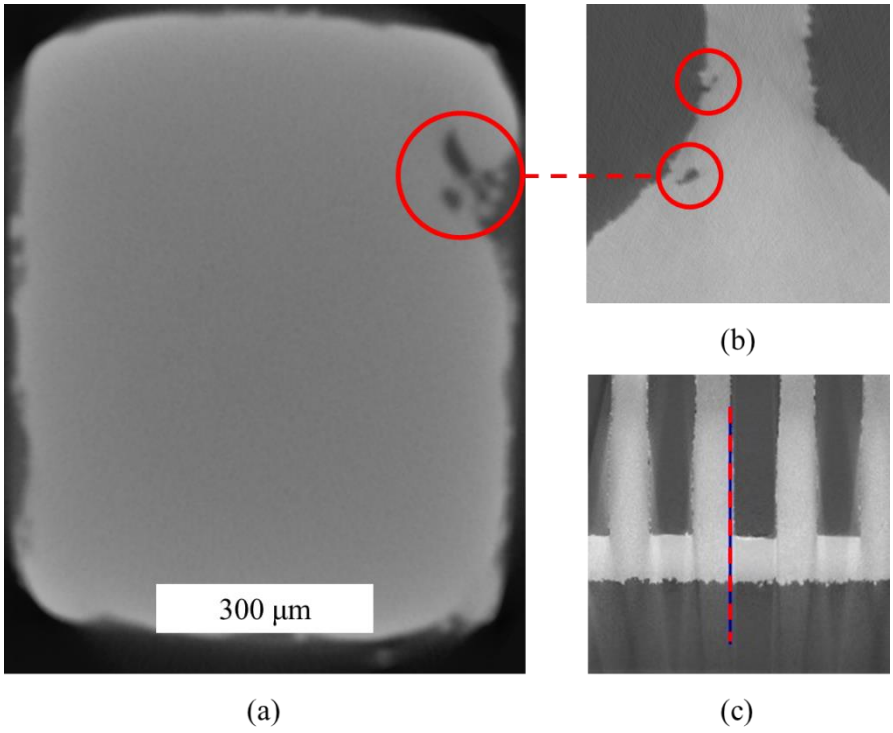

Figure 10: CT Images of a HIPed sample showing (a) a view normal to the build direction, (b) a side view of the surface crack, (c) the plane location of image (b)

The decrease in density due to the HIPing process may also be a result of insufficient time at aging, as presented in Wang's study **[41]**. Wang explained that during the HIPing process, the material is initially densified by the powder movement. Plastic deformation increasingly densified the material when the applied pressure becomes greater than the yield stress of the powder, as the particles are squeezed into voids and porous spaces. The final stages of the HIP process densified material by diffusion and powder creep mechanisms, further squeezing powder atoms in the residual porosity. These densification stages are founded on aging times. The aging times listed in the ASTM standard **[31]** used for the current material are 240 ± 60 minutes, and based on Wang's findings, aging times less than 4 hours at the applied pressure and temperature used here have produced relative densities less than 100%. The exact heat treatment schedule was not included with the material, so it is entirely possible that the HIPing process met the ASTM minimum requirements yet produced a part below the standard density.

Section 3.2: Statistics

The additive manufacturing process is known to produce parts with a wide array of mechanical properties **[13, 20, 42, 43]**, and the use of large data sets coupled with statistical analysis allows for stochastically determined minimum values to base designs on. Despite the fact that all mechanical properties in the current study meet or exceed the minimum requirements set by ASTM F3056 **[31]** given in Table 8, it is important to establish the limitations of the printed material and subsequent heat treatments. The use of Weibull distributions has been widely applied in previous studies **[20, 44-47]** to

estimate mechanical properties in a variety of materials. Due to its versatility, a statistical analysis using the 3-parameter Weibull distribution will be applied here to provide lower bounds for low-probability extreme value characteristics. Minitab ™ statistical software was used to conduct the Weibull distributions calculations. Equation 1 demonstrates how the 3-parameter Weibull cumulative distribution is determined:

$$P = 1 - e^{\left[-\left(\frac{\alpha-\gamma}{\eta-\gamma}\right)^{\beta}\right]} \qquad (1)$$

where *P* is the cumulative distribution, α is the function's input variable, β is the shape parameter, η is the scale parameter, and γ is the location parameter. The shape parameter is used to describe the slope of the Weibull probability plot: the greater the value the steeper the line becomes. The scale parameter describes the spread of the distribution, as a higher scale parameter yields an extended distribution in values. A 3-parameter Weibull distribution differs from the 2-parameter by employing the use of the location value. The location parameter, or threshold, sets the lower bound of the distribution and incorporates the same units as the input variable. The probability of an event happening below the threshold value is zero, explaining why this probability function is so widely used, especially in engineering. The Minitab software also provides a goodness-of-fit parameter determined by the chosen confidence interval for the data being analyzed. For this data set, an adjusted Anderson-Darling (AD) statistic is used in accordance with the 3-parameter Weibull probability distribution to determine the goodness of fit at a 95% confidence interval. The AD statistic is a measure of how far the range of values fall from the fitted line using a weighted squared distance. The tail of the distribution is given a larger weight to account for low-level outliers that may be present in the data set. The

Minitab software also uses the Anderson-Darling statistic to calculate the p-value **[48]**. For a 95% confidence interval, a p-value above 0.05 provides evidence that the null hypothesis should not be rejected. In this case, failing to reject the null hypothesis implies that the Weibull parameters, more specifically the threshold values, can be used as minimum design limits that are statistically sound.

Yield Strength at 0.2% offset	Tensile Strength	Elongation in 4D
275 MPa	485 MPa	30 %

Table 8: ASTM F3056 Minimum Tensile Properties

Figure 11 shows the 3-parameter Weibull plots of (a) yield strength, (b) ultimate tensile strength, (c) modulus, and (d) elongation at failure. Accompanying these plots are the Weibull parameters, the number of samples N, the Anderson-Darling statistic, and the p-value for each property in Table 9. Note that multiplying the listed p-values by 10 gives

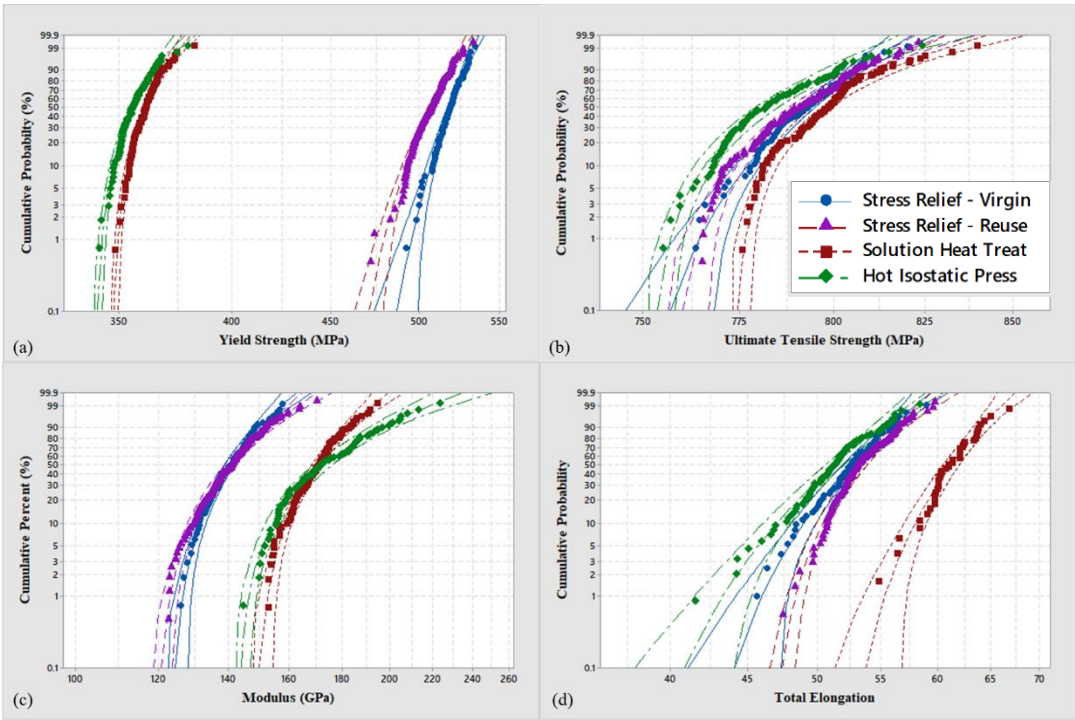

Figure 11: IN625 3-Parameter Weibull Distribution of (a) yield strength, (b) ultimate tensile strength, (c) Young's modulus, (d) elongation, plotted with line fits and 95% confidence bounds

	Sample	Shape	Scale	Threshold	N	AD	P-value
Yield Stress (MPa)	SR - Virgin	9.159	65.19	456	93	0.259	>0.500
	SR - Reuse	5.957	57.33	453.1	148	0.314	0.473
	SolHT	2.614	16.34	346.7	99	0.356	0.435
	HIP	2.571	18.15	339.9	94	0.320	>0.500
Tensile Strength (MPa)	SR - Virgin	4.848	51.64	744.5	93	0.202	>0.500
	SR - Reuse	2.928	38.42	756.4	149	0.566	0.111
	SolHT	2.125	28.92	773.2	99	0.830	0.032
	HIP	2.487	35.37	751.5	94	0.282	>0.500
Modulus (GPa)	SR - Virgin	2.815	20.07	122.7	93	0.216	>0.500
	SR - Reuse	2.659	24.91	118.8	147	0.299	>0.500
	SolHT	2.764	25.5	147.9	99	0.296	>0.500
	HIP	2.041	35.71	142.8	94	0.281	>0.500
Elongation (%)	SR - Virgin	5.097	12.68	40.79	70	0.180	>0.500
	SR - Reuse	3.267	7.857	46.43	126	0.485	0.18
	SolHT	4.727	10.69	51.33	43	0.432	0.228
	HIP	5.687	16.3	36.01	82	0.525	0.117

Table 9: IN625 Weibull parameters

the risk percentage. The spread in mechanical properties becomes much more obvious while viewing the cumulative distributions: both powders in the stress relieved condition have a much higher yield strength, the ultimate tensile strength values were grouped closely together, the Sol. HT showed the most elongation, and both solution and hot isostatic press heat treatments resulted in higher modulus values. The majority of the curves shown in Figure 11 are curved due to a logarithmic scale used on the y-axis but not the x-axis. The unscaled x-axis is used to show asymptotic behavior as the values converge towards the low-probability extreme values. Based on the AD statistics and p-values, the stress relieved virgin powder and HIP specimens displayed the most consistent yield strength, ultimate strength, and modulus values. The stress relieved virgin powder was also the only sample with a dependable goodness-of-fit statistic and p-value for the elongation results. The reused powder and additional heat treatments

introduced low probability outliers at the tails of the distribution, negatively effecting the line fit. Without rejecting the null hypothesis, the threshold values determined by the Weibull distribution provide solid guidelines for design. However, not all the Anderson-Darling metrics show evidence of a good fit due to the spread in the mechanical performance of the material. The lower limits set in the ASTM standard for this material **[31]** provide a minimum requirement well below any of the threshold parameters found in this study. However, the strength and modulus values measured are below other strength parameters mentioned in the literature **[37, 49-51]** as well as other findings that were part of this study **[52]**. The role of the sub-size tensile bar geometry on the decrease in mechanical properties will be addressed in the following sections.

Section 3.3: Powder Reuse and Build Location

Powder bed additive manufacturing processes, such as electron beam melting and laser powder bed fusion (LPBF), offer many advantages over other AM processes and classical subtractive manufacturing **[53]**. One of the benefits is that the unused print powder can be recycled and reused for another build. A study by Nandwana et al. **[54]** demonstrated that the nickel alloy Inconel 718 can sustain up to 6 reuse cycles without significantly altering powder properties or build chemistry. The same study concluded that reusing Ti-6Al-4V powder showed an increase in oxygen content and both powders displayed metallization after reuse. Other studies of the same materials, Inconel 718 **[33]** and Ti-6Al-4V **[55]**, showed that mechanical properties of these materials were not negatively affected by the recycled powder after 14 and 21 powder reuse cycles, respectively. In fact, the Ti-6Al-4V components revealed an increase in yield strength

and ultimate tensile strength without a decrease in elongation as a result of an increase in oxygen content between builds 6 and 21.

The test coupons in build 3 of this study were printed using recycled powder from builds 1 and 2. Analysis of the powder chemistry shown in Table 1 concluded there was no meaningful change in material characteristics after one reuse cycle. The stress-strain curves and average mechanical properties, Figure 8 and Table 6, respectively, reveal minimal deviation from one another, however, after statistical analysis, the recycled powder had a larger spread of data and more low probability irregularities. These slight differences are attributed to a larger sample population and not a change in material behavior, as larger data sets reveal more details about natural variability **[42]**. It is hypothesized that increasing the number of reuse cycles would not substantially affect the observed mechanical properties, however, this claim is outside the scope of this work and requires a more in-depth study.

The location on the build tray and the orientation of the tensile bar racks were two additional process parameters tracked in this study, as mentioned in Chapter 2, to determine what affects the recoater blade and gas flow may have on mechanical properties. Tensile bar orientation was not included in this study as the arrays were printed with the tensile axis parallel to the build direction. Previous studies of the same LPBF material **[50, 52]** showed a dependency on tensile axis orientation to the build direction; a tensile axis parallel to the build direction resulted in lower strength and higher ductility when compared to a perpendicular tensile axis. Based on these findings, the results analyzed here provide conservative estimates for expected strength properties. Figure 5 shows all three build layouts with corresponding sample numbers and each of

the individual rack's mechanical properties are listed in Table 10. Correlating the listed values to the location on the build plate shows that there isn't a strong relationship between the gas flow direction or the recoater path of travel to mechanical properties. There is, however, one exception. Sample 1103, a HIP specimen located at the top right of build plate 1, shown in Figure 5 (a), had a lower average modulus than the rest of the HIP samples while the strengths and elongation values remained constant. The change in modulus is presumably due to a difference in microstructure and not a result of its location on the build tray. The effect of microstructure on modulus values will be addressed in the following section.

Part Number	Heat Treat	Area (mm^2)	YS (MPa)	UTS (MPa)	Modulus (GPa)	Ductility (%)
1101	SR	1.17	515	790	142	52
1104	SR	1.17	514	786	137	51
4101	SR	1.17	523	799	145	52
4104	SR	1.17	519	793	138	53
7101	SR	1.17	500	787	142	53
7102	SR	1.17	503	786	150	54
7103	SR	1.15	506	793	144	54
7104	SR	1.16	502	784	131	53
7105	SR	1.15	518	804	137	54
7106	SR	1.16	508	789	142	53
1102	Sol HT	1.15	364	806	172	62
1105	Sol HT	1.16	360	795	175	61
4102	Sol HT	1.17	360	797	172	62
4105	Sol HT	1.16	360	794	163	61
1103	HIP	1.15	359	788	159	50
1106	HIP	1.17	355	779	185	49
4103	HIP	1.20	353	778	165	54
4106	HIP	1.18	358	787	186	52

Table 10: IN625 mechanical properties of individual tensile racks

Section 3.4: Microstructure

Determining the role that the microstructure plays in mechanical performance is key in understanding how the various heat treatments will affect mechanical behavior. The images shown in Figure 6 were further analyzed using Oxford Channel 5 software to determine grain size, orientation, and texture within the samples.

The Hall-Petch relation is used to describe a method of material strengthening by decreasing the grain size of the material **[56]**. Grain boundaries act as obstacles and impede dislocation motion, requiring more energy for dislocations to move. Disrupting the movement of dislocations hinders the onset of plastic deformation, thus increasing the yield strength of a material **[38, 56]**. A decrease in grain size within the material increases the number of grain boundaries present and based on the Hall-Petch relation, the yield strength of the material increases. Equation 2 shows the Hall-Petch equation

$$\sigma_y = \sigma_0 + kD^{-\frac{1}{2}} \qquad (2)$$

where σ_y is the yield stress, σ_0 is a frictional stress required for dislocation movement, k is the strengthening coefficient, also known as the Hall-Petch slope, and D is the grain size. Shown in Table 11 are the grain size measurement results and corresponding yield stress values for the stress relieved, Sol. HT, and HIP samples. The grain sizes measured by the Channel 5 software show a strong interaction between a decrease in grain size and an increase in yield stress. The frictional stress and strengthening coefficient values published by Gao et al, **[57]**, 105 MPa and 1380 MPa $\sqrt{\mu m}$, respectively, show a correlation between published data and the results observed in this study. Figure 12 plots the yield stress versus grain size of published data and the current values. While the Hall-

Petch relation correlates the difference in yield stress to grain size relatively well, it doesn't provide a complete story. Other factors, such as the presence of precipitates, may also be a factor in the onset of plastic deformation.

Sample	Data Set Size	Avg. Grain Size (μm)	$D^{-\frac{1}{2}}$ $(mm^{-\frac{1}{2}})$	Yield Stress (MPa)
SR – Virgin	1157	11.8	29.1	518
SR – Reuse	1240	12.2	28.6	508
Sol HT	954	21.6	21.5	361
HIP	978	24.4	20.2	356

Table 11: IN625 grain sizes and yield strength

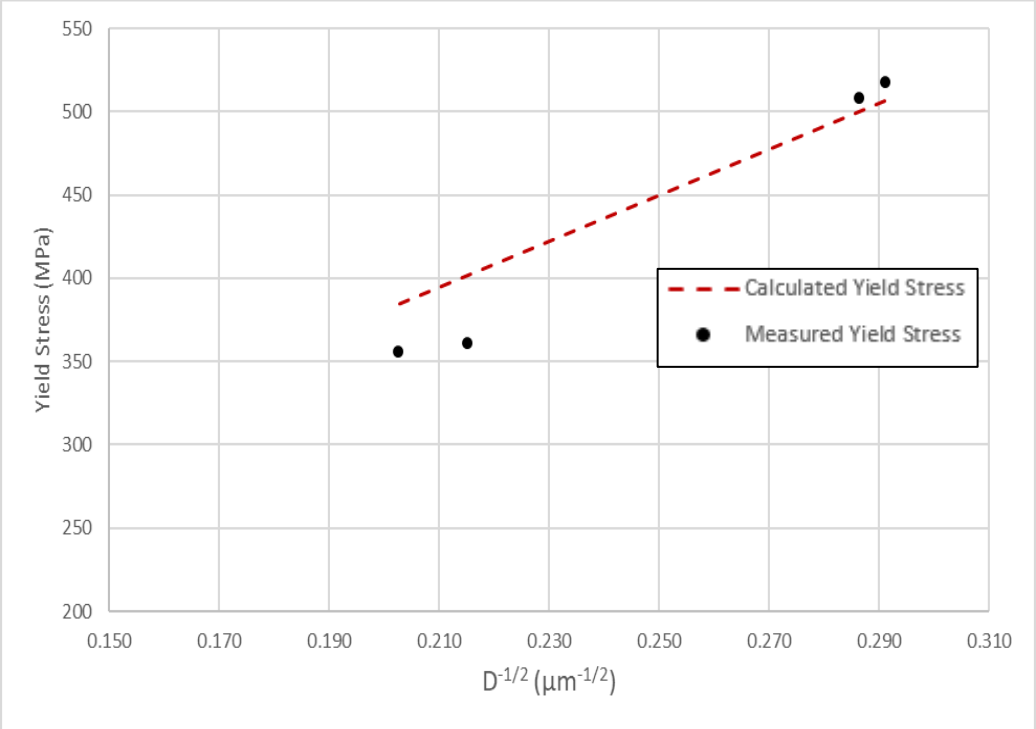

Figure 12: Yield stress versus grain size of published data and the results found in this study

In polycrystalline materials, like the nickel alloy presented here, the elastic constants are regulated by the distribution of grain orientations within the material **[38]**. The deformation in each grain is dependent on the deformation of its neighboring grains, and the local stress and strain are equal to the mean values of the grains in that region. The anisotropy of materials produced by additive manufacturing is well known **[58]** and the heterogeneity of the microstructures can affect the elastic constants. The epitaxial and columnar grain growth of the stress relieved samples, shown in Figure 6, suggest anisotropic properties, as mentioned in the literature **[59, 60]**. The solution and hot isostatic press heat treatments homogenized the microstructure, resulting in a more equiaxed grain formation. To better quantify the observed changes in grain morphology, the grain orientations were plotted using inverse pole figures (IPF). Shown in Figure 6 are the densities of grain orientation, with red representing a higher orientation density. Based on the IPFs, the stress relief samples show some texture in the <001> direction. The Sol. HT sample had texture in the <101> and <111> orientations, with clusters scattered throughout the lower portion of the IPF. The HIP shows a preference for the <111> direction, with some orientation in the <304> direction. Equation 3 can be used to correlate the grain texture and expected modulus values:

$$\frac{1}{E_{ijk}} = S_{11} - 2\left(S_{11} - S_{12} - \frac{1}{2}S_{44}\right) \times (I_{i1}^2 I_{j2}^2 + I_{j2}^2 I_{k3}^2 + I_{i1}^2 I_{k3}^2) \qquad (3)$$

where E_{ijk} is the modulus in the [ijk] direction, I_{i1}, I_{j2}, and I_{k3} are the direction cosines of the [ijk] direction, and S_{11}, S_{12}, and S_{44} are the elastic compliances. In correlating the average modulus values to the grain orientation, the results presented differ from the anticipated orientation distributions. The observed modulus values were ~140 MPa for

both the virgin and reused powder SR samples, and ~170 MPa for the Sol. HT and HIP samples. Nickel, the primary element in IN625, has a very high anisotropic ratio based on the stiffness matrix for the material **[38]**. The Zener ratio, a well-known measure of elastic anisotropy in cubic crystals **[61]**, is defined as:

$$Z = \frac{2c_{44}}{c_{11} - c_{12}} \qquad (4)$$

where c_{11}, c_{12}, and c_{44} are elastic stiffness constants. A Zener ratio value of 1 indicates elastic isotropy. Using the reported elastic stiffness constants **[38]**, nickel has a Zener ratio of 2.54, indicating a high level of anisotropy. This ratio suggests that the differences in modulus values are possibly due to a change in preferred grain orientation between the heat treatments.

Using the elastic compliances for nickel and the major alloying elements **[38]**, chromium, molybdenum, and niobium in Equation 3 yields elastic modulus values of 164 GPa, 234 GPa, and 271 GPa along the [100], [101], and [111] direction cosines, respectively. The values used in the calculations are given in the appendix. While these values are higher than those found in this study, 140 GPa for the stress relieved and ~170 GPa for the solution annealed and HIP samples, this method is employed to show the anisotropic behavior of the material and the dependency of elastic properties on preferred grain orientation. The modulus value for IN625 is around 200 GPa as reported in the literature **[39, 41]**, and the observed decrease in stiffness is likely due to surface crust and porosity. It is hypothesized that the stronger texture observed in the Sol HT and HIP samples explain the increase in modulus when compared to the lack of texture in the stress relieved materials. The 3 times random <111> orientation in the HIP sample, along

with 3 times random <101> orientation for the Sol HT material, may provide more stiffness for the material than the <001> orientation observed in the stress relieved samples. The observed columnar grains may also play a role in the anisotropic elastic stiffness. Hasebe et al. **[62]** have shown a decrease in Young's modulus in materials with a directionally solidified microstructure (columnar grains) when compared to the same material with an equiaxed microstructure. Chlebus et al. **[63]** have also shown modulus dependency on directional solidification of grains within additively manufactured Inconel 718. The findings presented by Chlebus show a decrease in modulus, yield strength, and ultimate tensile strength in samples with grains elongated in the tensile direction versus samples with elongated grains orientated 45° and 90° to the tensile direction. Based on the results presented in the literature and those found in this study, the anisotropic behavior of the material is the probable cause of the observed variation in elastic modulus.

The mechanical properties reported at the start of the chapter showed the lowest ductility values belonging to the HIP samples. While the density calculations provided a potential explanation to the observed anomaly, the results found were not strong enough to draw a sound conclusion. As introduced in the first chapter, the presence of precipitates in IN625 alloys has been well documented and it has been shown they play a role in mechanical performance. Numerous studies highlight the effect of temperature and time at aging as they significantly alter the formation and dissolution of precipitates. SEM imaging and EDS microanalysis were conducted with the use of a Zeiss GeminiSEM to better understand the role of precipitates on the observed mechanical properties in this study. As seen in Figure 13, the presence of precipitates is not obvious

at this magnification. Other studies have shown precipitates with plate-like morphology in the interdendritic regions of stress relieved LPBF IN625 that were found to be δ-phase (Ni_3Nb) with the use of TEM **[10]**. The determination of precipitates in the stress relieved material, however, is beyond the scope of this work.

Figure 14, an SEM image of a solution treated specimen, shows a small population of precipitates, displayed as bright white marks. Various publications, namely Marchese **[49]**, Lass **[10]**, and Keller **[16]**, have shown the existence of Nb and Mo-rich carbides in the solution annealed IN625. EDS mapping of the current material, shown in Figure 15, agrees with the published results, as the Nb and C maps show the most conformity with the white spots when superimposed over the SEM image. The Mo signal, while not nearly as strong as the one produced by Nb, does show some correlation with the precipitate locations. While TEM has not been performed, it is hypothesized that

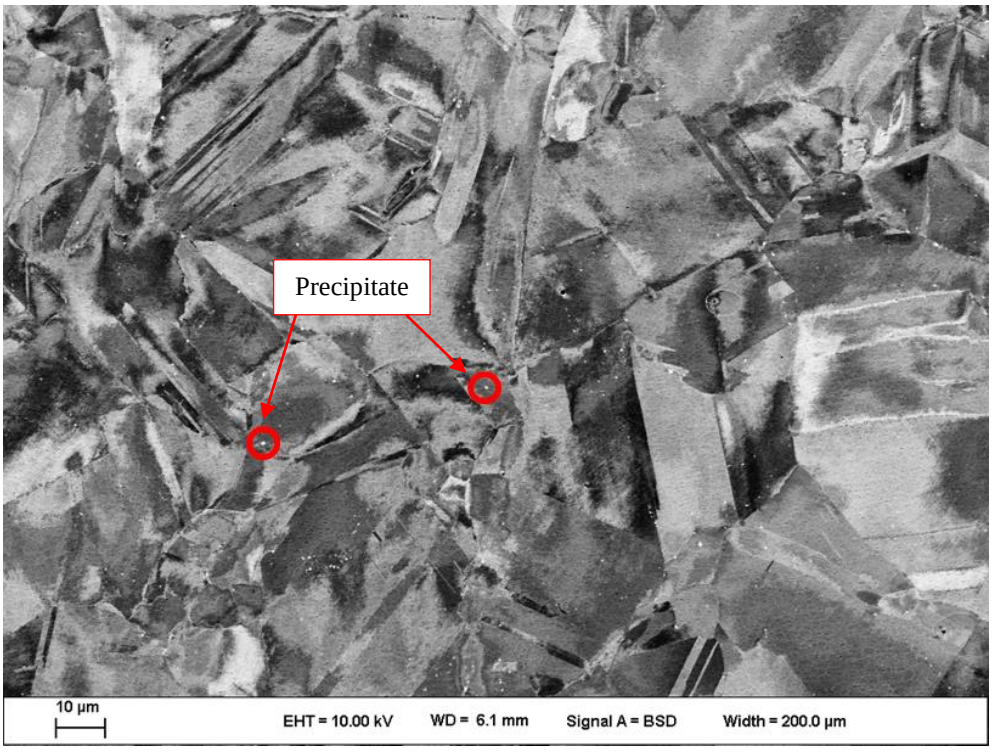

Figure 14: SEM Image of a Sol HT sample, showing signs of precipitation, circled in red

the precipitates present are Nb and Mo-rich carbides, as the Ni signal is weak in the precipitate locations **[10]**. The scatter in precipitates, as displayed in Figure 14 and Figure 15, shows no strong inclination towards a preferential location.

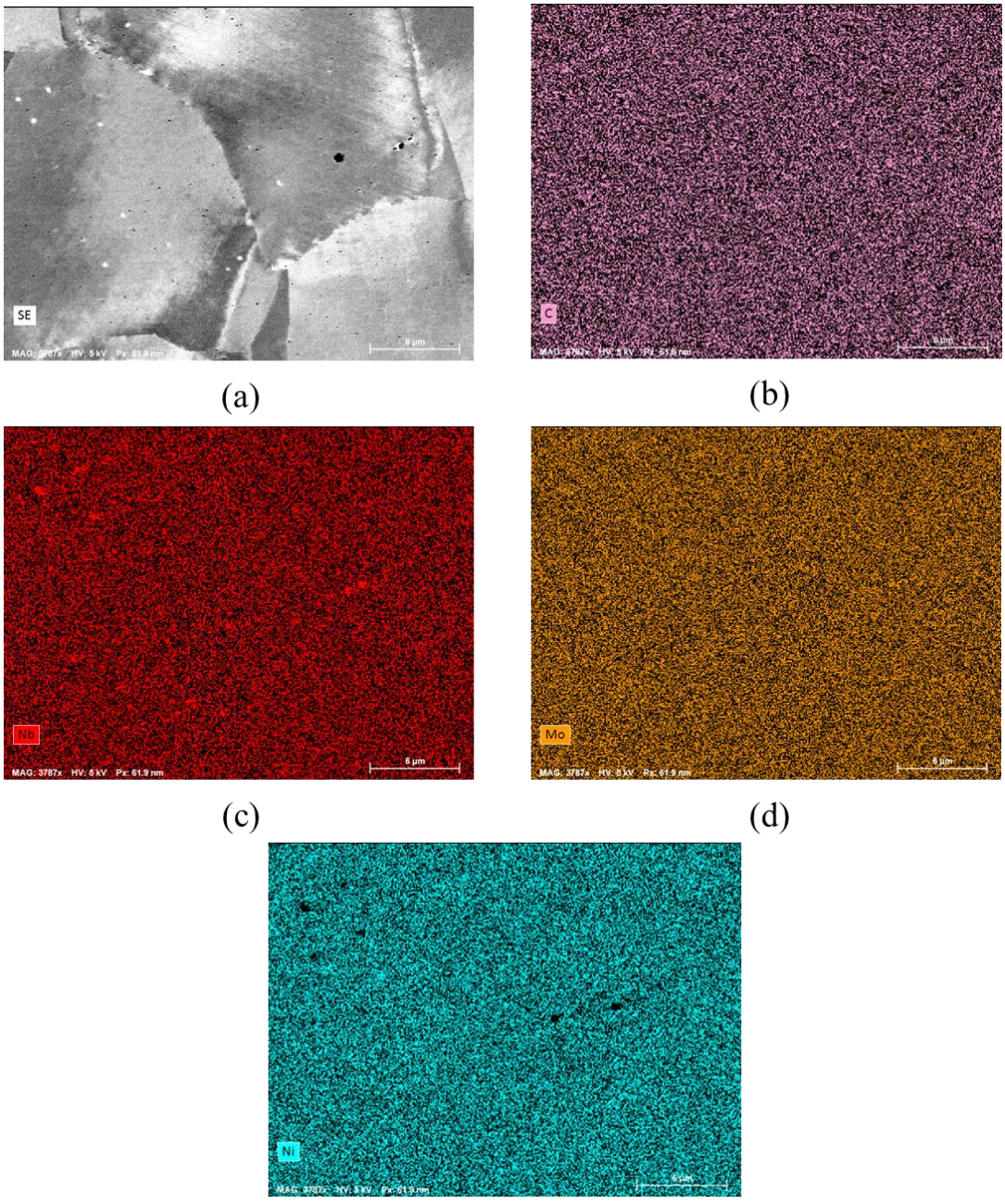

Figure 15: EDS maps of a Sol HT sample, showing (a) SE map, (b) C map, (c) Nb map, (d) Mo map, (e) Ni map

The precipitation of hot isostatic pressed laser powder bed fusion IN625 is not well documented in the literature, however, Rao **[64]** concluded that the existence of brittle oxides and carbides in a HIPed Inconel 718 led to low ductility. Wang et al **[41]** showed the nucleation of MC (Nb, Ti) carbides along prior particle grain boundaries (PPB) in an Inconel 625, as PPB's are a common defect produced during the HIPing process cooling stage **[65]**. An SEM image of the HIP sample reveals a much greater presence of the precipitates shown in the Sol HT sample, as displayed in Figure 16. Larger precipitates appear more frequently along the grain boundaries, however, transgranular precipitates are also observed throughout the image. EDS analysis of the HIP sample, displaying the same element maps used in Figure 15, reveals strong Nb signals in the precipitate locations. The weak Ni signal, coupled with an increase in C

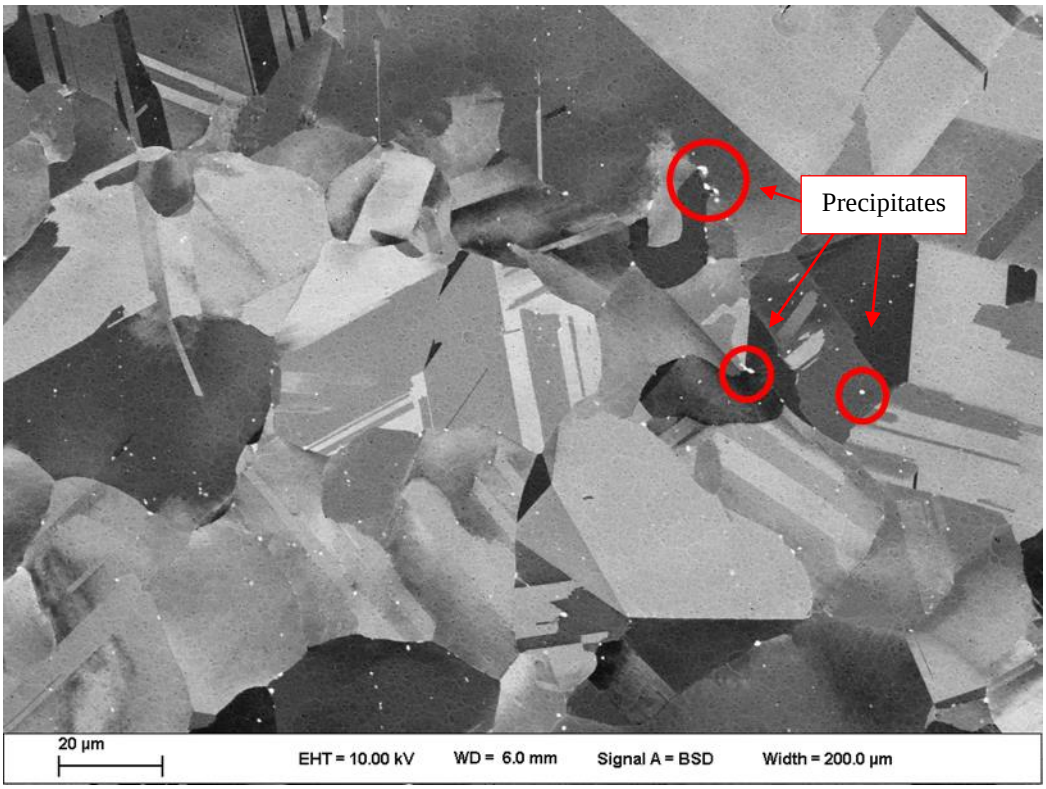

Figure 16: SEM image of a HIP sample, showing signs of precipitation, circled in red

signal strength in line with the precipitate position, suggests that the precipitates are in fact Nb-rich carbides. Figure 17 shows the EDS maps of a HIP sample.

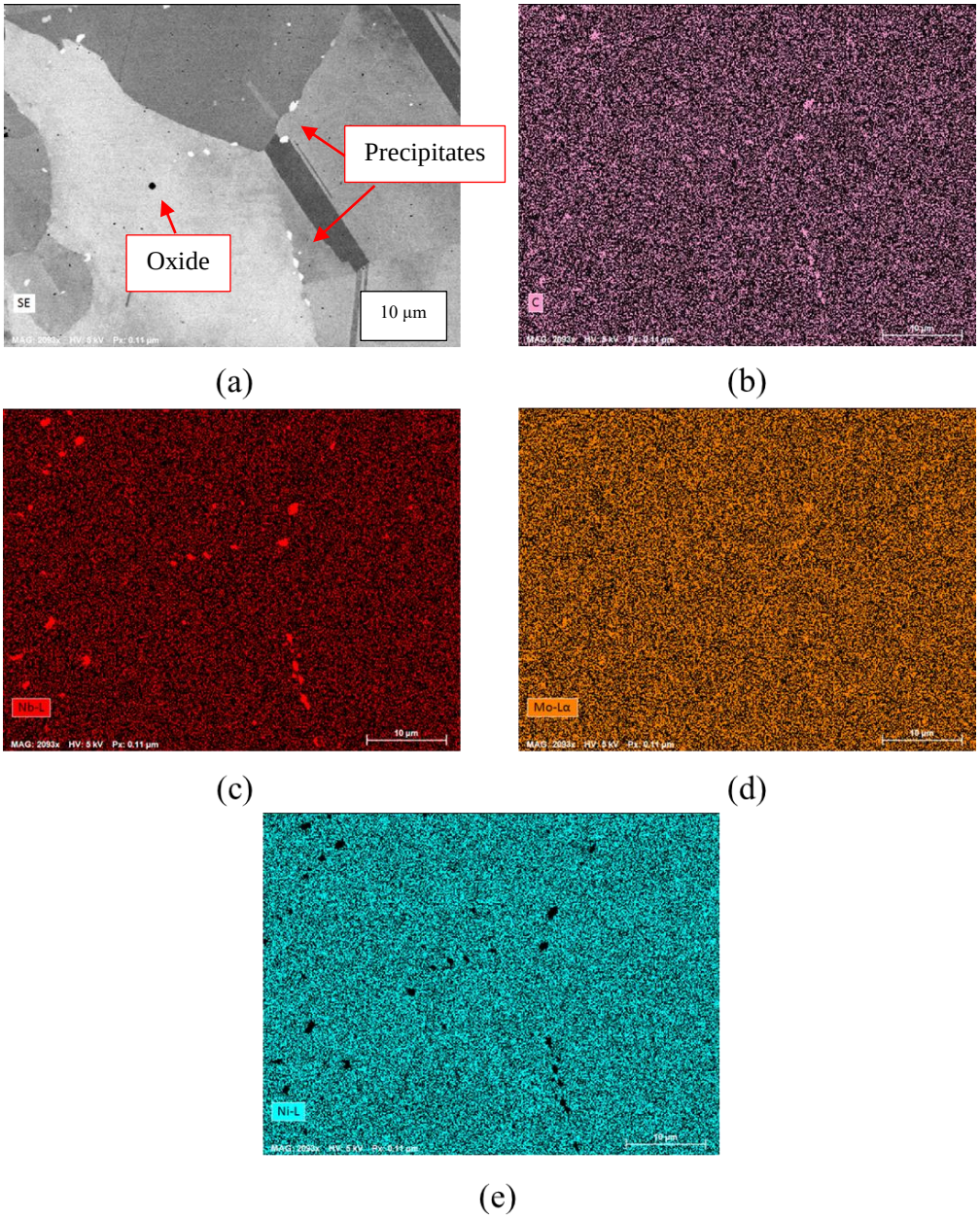

Figure 17: EDS maps of a HIP sample, showing (a) SE map, (b) C map, (c) Nb map, (d) Mo map, (e) Ni map

The EDS analysis of the solution annealed and hot isostatic pressed samples were conducted to determine if there was an obvious difference in precipitation presence

between the two materials. The scales used for EDS mapping of the two samples are inconsistent: The Sol HT image was taken at a magnification of nearly double that used to image the HIP specimen. The variation in magnification is presented to show that while some precipitates are observed in the solutioned material, the size and density are less than those observed in the HIP sample. The average precipitate size of those observed in the Sol HT sample, as displayed in Figure 15, is approximately 340 nm in diameter. The average HIP precipitate size measured using those found in Figure 17 (a), is given as 900 nm in diameter. The abundance of precipitates along grain boundaries, in addition to the increase in the size of the precipitates found in the HIP sample, is attributed to the preferential nucleation along grain boundaries. Increasing the aging time and cooling rate used in the HIP process is likely to reduce the number of precipitates formed in the material. Longer diffusion time at elevated temperature has shown to reduce PPBs and increasing the cooling rate restricts carbide precipitation **[64, 66]**. Future research would be needed to quantify this hypothesis.

Originally thought to be pores, Figure 15 (a) and Figure 17 (a) show oxides present in the SEM images of the Sol HT and HIP samples. EDS microanalysis was used to determine the components of these voids. Figure 18 shows an SEM image accompanied with the EDS microanalysis of the void space, composing primarily of oxygen and aluminum. Studies have shown that the formation of stable oxides is common in Ni-super alloys, especially when exposed to oxygen environments, and the results found in this study agree **[41, 64, 66]**. TEM analysis is needed to confirm, however, the EDS results provide compelling evidence that the observed oxide is Al_2O_3. While the presence of oxides in the SR samples is not shown here, it is proposed that they exist in

both powder conditions. The higher density found in the reused powder, as presented in Table 7, may be due to a decrease in oxides, as builds 1 and 2 experienced higher oxygen content during printing. Oxide formation due to the presence of oxygen during fabrication is a future topic of research.

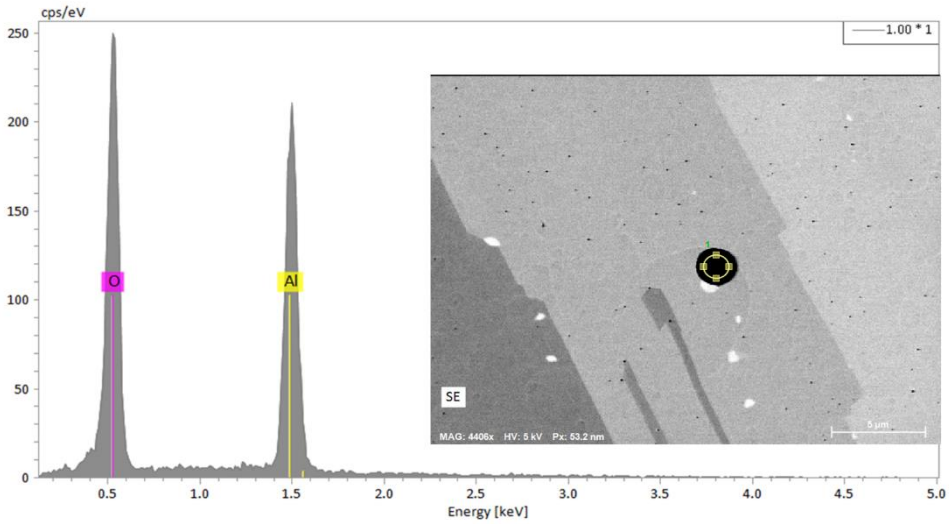

Figure 18: EDS analysis of a void showing the element composition

The abundance of precipitates found in the HIP sample, especially those located along the grain boundaries, are presented as the main contributor to the decreased ductility. The carbides nucleate along the PPBs and coarsen as the material cools. The carbides then block dislocations, strengthening the material while limiting ductility. As Rosalie has shown **[67]**, increasing the size and density of precipitates further strengthens the material at the expense of ductility. The HIPing process, however, is employed to increase the elongation at failure while reducing the ultimate strength, justifying the need for an adjustment in heat treatment parameters. The brittle oxides observed in the material likely contribute to a decrease in ductility, however, it is doubtful they played a

significant role, as they are observed uniformly in both the Sol HT and HIP samples and are expected in the SR specimens as well.

Section 3.5: Sub-Size Effect and Fracture Surfaces

The mechanical properties measured in this study, while exceeding the minimum requirements for this material **[31]**, all displayed lower strength values than those of the standard tensile size specimens that were included in the builds, as reported by Martukanitz **[52]**. The size effect has been well documented in the literature **[13, 68-70]** and is explained here as a reason for the lower yield strength and ultimate tensile strength when compared to conventionally sized tensile bars. The over-estimation of the high-throughput area measurement system, coupled with surface roughness causing a decrease in effective load-bearing area, are the primary factors that reduce the observed strength values. Salzbrenner **[13]** corrected for surface roughness by reducing the measured the cross-sectional areas with surface roughness measurements and found that while the strength values increased, they didn't match the properties of the wrought material in the study. Equation 5 represents the engineering stress calculated corrected for surface roughness:

$$\sigma_{\text{corrected}} = \frac{F}{(w-2R_p)*(t-2R_p)} \qquad (5)$$

where F is the force, w is the measured width, t is the measured thickness, and R_p is the average peak roughness. Applying the same process, using the surface roughness measurements given in Table 3, increased the strength values. However, the corrected properties still fall short to those of the standard size tensile bars. Given in Table 12 are

the original ultimate strengths determined during testing, the sub-size strengths corrected for surface roughness using Equation 5, and the standard size strength values taken from Martukanitz's study **[52]**. The surface roughness correction, while it brings stress values closer to those of the standard size tensile bars, does not consider voids or porosity that may initiate premature failure within the sub-size samples. Dislocation density may also play a role, and although it is outside the scope of this study, it is possible that the dislocation density near the edge of the material is a factor in lower strength, as both the sub-size and standard size tensile bars show similar elongation percentages. Studies have shown that grains near the surface of materials have a reduced dislocation density due to free surface dislocation escape **[68, 70]**. The inherent surface roughness of additively manufactured materials, in addition to the limited cross-sectional area of the tensile bars used, may have contributed to free surface dislocation escape, lowering the ultimate strength of the material. The modulus values observed in this study were also considerably lower than those reported in the literature **[39]**. Previous unpublished studies using the high-throughput procedure, however, have shown the modulus values of machined samples on par with standard size results. Removing the surface roughness via machining reduces the stress concentration sites at crevices, increasing the strength and modulus values of the material.

Heat Treat	Sub-Size UTS	Corrected Sub-Size UTS	Standard Size UTS
SR	791	898	932
Sol HT	798	903	929
HIP	783	864	922

Table 12: Corrected ultimate strengths

The CT scans of the HIPed sample, given in Figure 10, demonstrated no sign of voids or porosity present within the material other than the indicated surface cracks. To further scrutinize the reduced ductility measurements, as well as investigate the presence of voids not detectable by CT imaging, SEM images were taken of the fracture surfaces from each heat treatment. Figure 19 shows the fracture surface of a sample from each treatment parameter. In comparing these images, there are no obvious features that suggest voids or porosity are the reason for the lower than expected elongation values in the HIPed samples. In fact, magnified portions of the same images display larger voids in the stress relieved and solution treated samples than in the HIP material. These larger

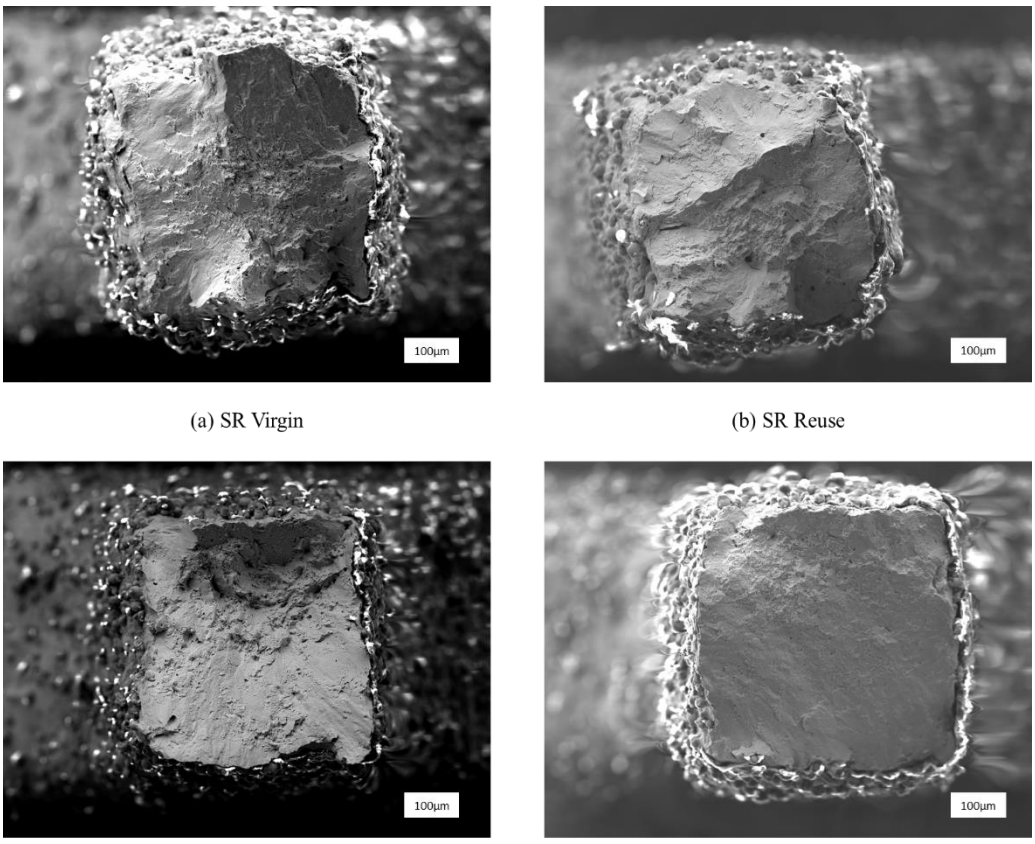

(a) SR Virgin (b) SR Reuse

(c) Sol HT (d) HIP

Figure 19: IN625 fracture surfaces

voids are determined to have formed due to entrapment of gas during the AM process, as gas porosity is inherently spherical in nature. Figure 20 displays focused sections of the fracture surfaces given in Figure 19. Ductile dimples are present in every specimen, commensurate with ductile failure modes. These dimples, formed as microvoids, nucleate while the material is strained, eventually causing failure as the voids coalesce. Cleavage planes, indicative of brittle transgranular fracture, are observed surrounding porous spaces in the SR samples and near cracks in the Sol HT and HIP specimens. The evidence of brittle failure, while present, is significantly dwarfed by the ductile dimples.

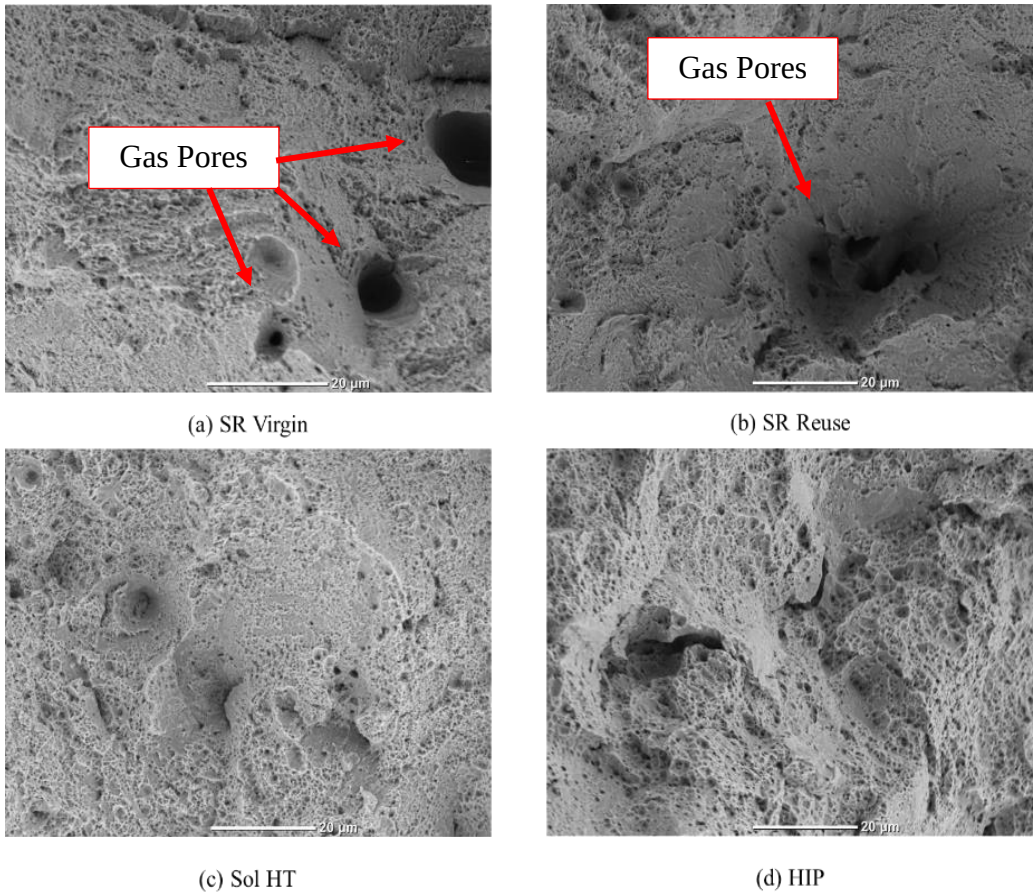

Figure 20: High magnification IN625 fracture surfaces

Chapter 4 – AlSi10Mg Alloy Results

Presented in this chapter are the density, hardness, and impact toughness results and how they can be used to determine print performance without the need to test actual components. The mechanical properties and statistically determined extreme values are also introduced, followed by a fractographic analysis of the observed characteristics.

Section 4.1: Density, Hardness, and Impact Toughness

The density, hardness, and impact toughness results obtained as part of the component qualification process are presented here and show that these methods provide an accurate representation of anticipated mechanical properties. Each of the two build plates provided 8 Charpy samples, allowing for 16 total measurements to determine the variability in results. The average density of Charpy samples on the first build plate was 2.6481 g/cm^3, while the density for the second build plate was 2.6477 g/cm^3. Slight variability is to be expected, however, the accuracy and repeatability of the acceptance testing procedure and equipment used produced density measurements with an error between individual sample measurements of less than 0.02%. The relative density of the two build plates, determined using a reference density of 2.68 g/cm^3 as reported in the literature **[8, 71]**, are calculated at 98.8% dense. Values less than 100% dense indicate the presence of internal porosity within the material. The measured values in this study are similar to or better than densities reported in the literature of stress relieved AM AlSi10Mg **[9]**, however, supplementary studies have shown an improvement in density by adjusting the process parameters **[8, 17, 71]**. Porosity within any additively manufactured material can be attributed to a variety of flaws including lack of fusion

defects, pores caused by trapped gases, keyhole porosity, and voids present within the powder that remain after the melting process. The dominant modes of failure observed in this study are primarily linked to a substantial amount of lack of fusion defects, with some gas porosity present. The amount of porosity, and the detrimental effects on mechanical performance, will be discussed later in the chapter.

The hardness tests of each Charpy bar following density measurements showed minimal variation both within and between builds, suggesting nominally identical mechanical properties are to be expected. The average Rockwell B hardness values for both builds are 44 HRB. Following hardness measurements, the samples are v-notched, and impact tested to determine the amount of energy absorbed by the material. Both builds absorbed an average of 10 ft-lbf of energy, with a minimal spread between values. To better understand the amount of variation in measurements, the hardness and impact energy values are plotted with density to show there is a linear trend: an increase in

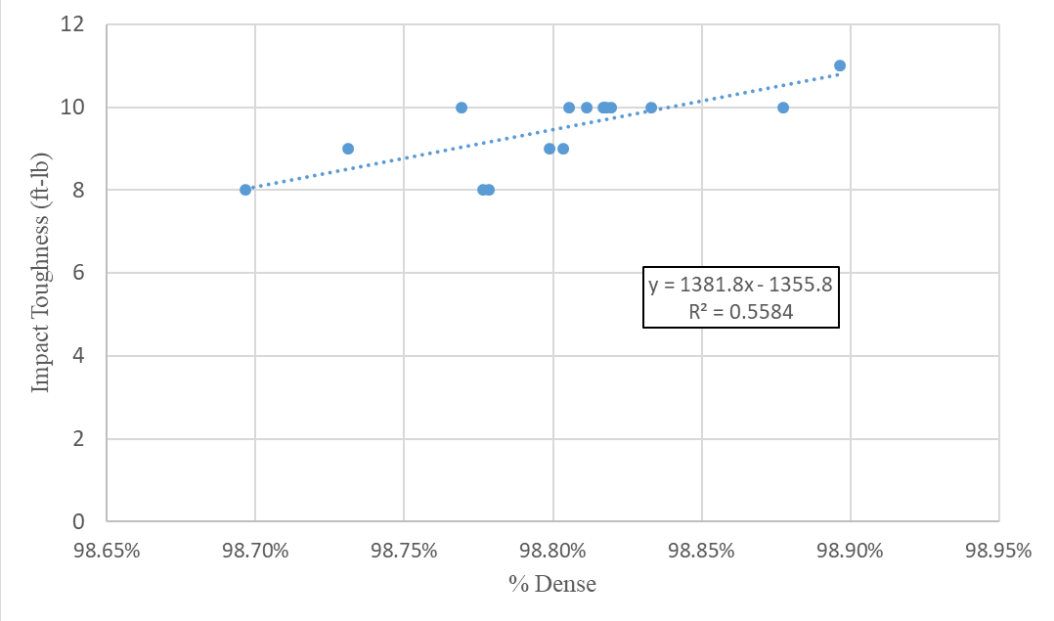

Figure 21: AlSi10Mg Charpy impact toughness vs density with linear regression line

density yields higher Charpy impact toughness values, as shown in Figure 21. Higher density levels indicate fewer pores are present, providing more material that a crack must travel through before the sample fails, thus increasing the energy absorption. The R^2 value of 0.56 shows the acceptance testing procedure, more specifically the density and impact toughness values, are a good indication of build quality. The presence of pores may negatively affect the hardness measurements as well, however, the low R^2 value of 0.13 in Figure 22 suggests otherwise. Hardness measurements test microstructure, and the results presented here show that the non-correlation between hardness and density proves porosity is the major factor in Charpy toughness, not microstructure.

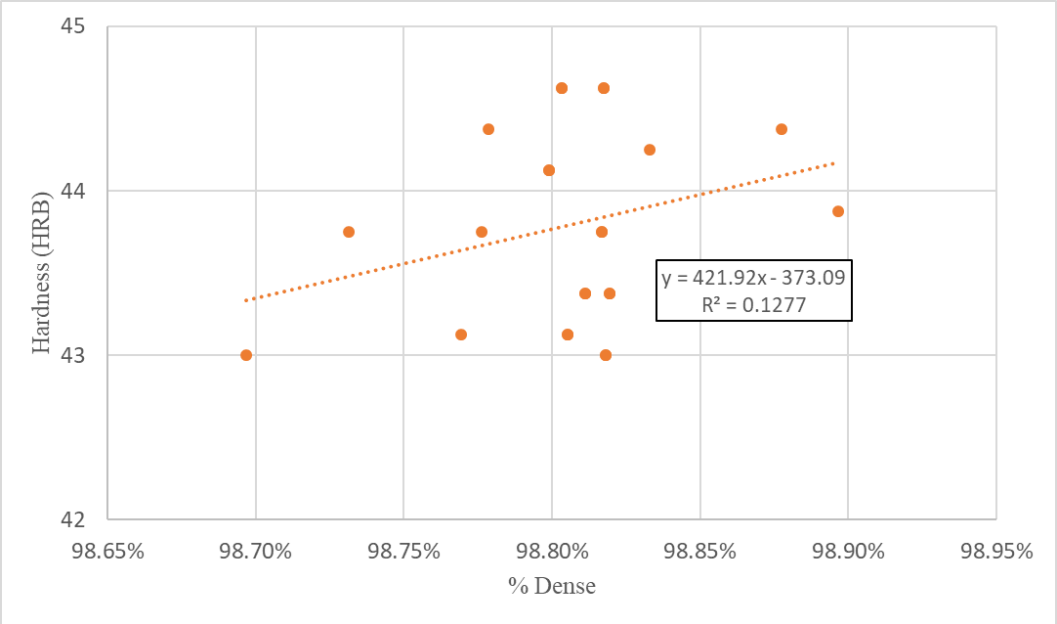

Figure 22: AlSi10Mg Rockwell B hardness vs density with linear regression line

The density, hardness and impact toughness values found in this study vary from those reported in a similar study by Kempen **[8]**, who reported higher density and hardness values but lower impact energy absorption. Kempen et al.'s higher density is attributed to process optimization by re-scanning each layer in an alternate pattern.

Finfrock **[9]** presented lower hardness values than those found by Kempen as well as those characterized in this thesis, along with a decrease in density. Based on these results, coupled with those reported by Kempen and Finfrock, a decrease in density caused by inherent porosity plays a key role in mechanical performance.

Section 4.2: Mechanical Properties

The AlSi10Mg tensile bars were printed in racks of 40 and tested using the high-throughput procedure described in Chapter 2. A small portion of the individual bars on each rack were bent during shipping and removed prior to testing, as the goal of this study does not include analyzing defects caused by factors external to processing. Figure 23 shows the compiled stress-strain curves of the two racks from each build (~140 specimens). Previous work using the high-throughput testing procedure on the AlSi10Mg alloy has shown a significant amount of variation in ductility, as seen here, so the unload loop for modulus determination was set at 0.5% strain in an attempt to obtain data prior

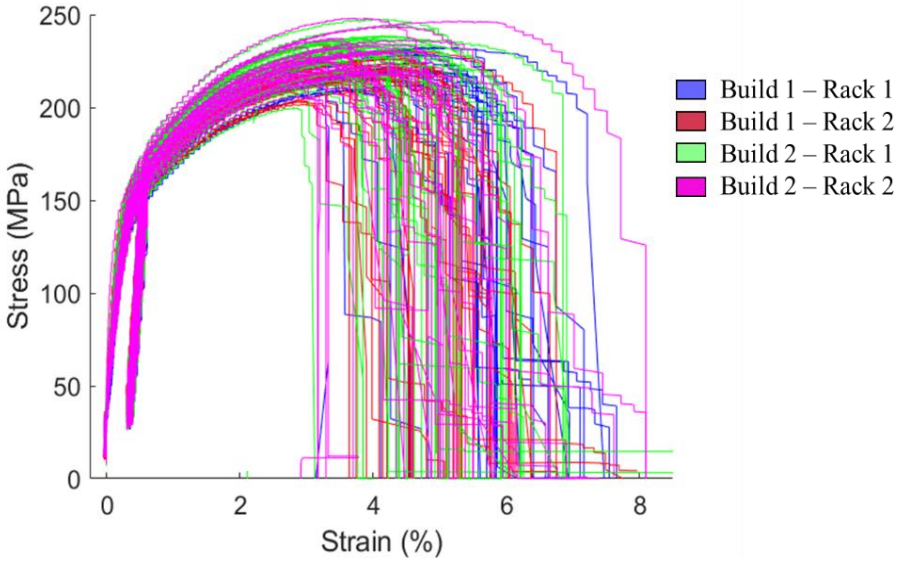

Figure 23: AlSi10Mg stress-strain curves

to failure. There is no clear indication of superior mechanical performance as each rack from both builds display a similar amount of variation in properties. Table 13 lists the average cross-sectional area, modulus determined from the unload loop, yield strength, ultimate strength, and ductility from each rack tested. The extremely low modulus values may be due to the amount of porosity present in the material. Pores deform during loading causing microplasticity, leading to unrecoverable deformation and reducing the modulus determined during unloading. Finfrock et al. **[9]** presented a relationship between unloading modulus and porosity; increasing the porosity in a sample by 8% decreased the modulus by more than 60%.

Sample	Num. of Specimens	Area (mm^2)	Modulus (GPa)	Yield Strength (MPa)	Ult. Tensile Strength (MPa)	Elongation at Failure (%)
Build 1 – R1	33	0.80	47 ± 2	152 ± 4	221 ± 7	5.5 ± 1.0
Build 1 – R2	35	0.79	47 ± 2	156 ± 5	220 ± 7	5.1 ± 0.8
Build 2 -R1	38	0.77	49 ± 3	160 ± 7	228 ± 10	5.0 ± 1.0
Build 2 -R2	36	0.77	49 ± 3	158 ± 6	227 ± 9	5.0 ± 1.0

Table 13: AlSi10Mg mechanical properties

The mechanical properties found by Finfrock et al. of the same material in the stress relieved condition were lower than those observed in this study and may be attributed to a higher porosity in their material **[9]**. The average reported properties in Finfrock et al. were ~35 GPa for modulus, ~165 MPa for ultimate strength, and ~4% elongation at failure. On the other hand, the mechanical performance shown in Kempen's study, more specifically the strength and stiffness of the material, out-performed the current results considerably **[8]**. The values given were ~68 GPa for stiffness, ~396 MPa for ultimate strength, and ~4% ductility. It is evident that a large amount of variation is

present in the AlSi10Mg material, so applying the statistical determination of minimum mechanical properties introduced in the Inconel 625 chapter is warranted.

Figure 24 shows the (a) yield strength, (b) ultimate tensile strength, (c) modulus, and (d) total elongation 3-parameter Weibull distributions of the AlSi10Mg material. The most variation in mechanical properties is observed in the yield strength values, as the spread in data is more pronounced in the Weibull plot. Rack 1 from build plate 2, labeled as Build 2 – R1, shows more low-probability yield and ultimate tensile strength values, as well as lower elongation at the tails of the Weibull distributions. These anomalies are likely linked to individual tensile bars with increased inherent porosity and will be discussed in more detail in the following section. Table 14 contains the Weibull parameters corresponding to the plots shown, listing the shape, scale, threshold value,

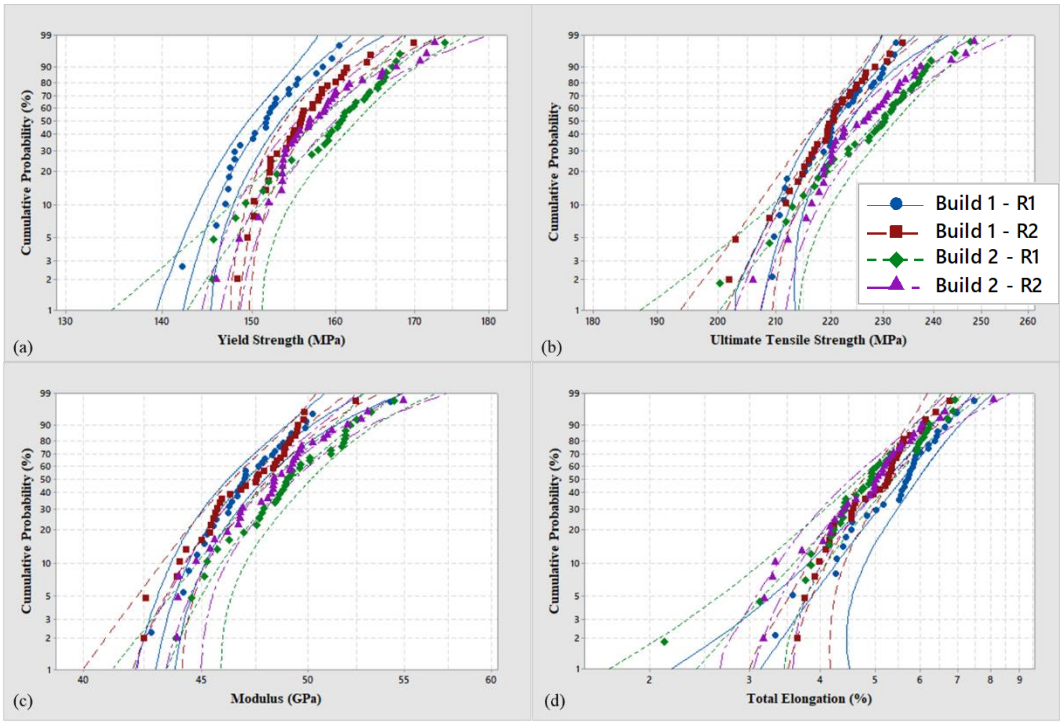

Figure 24: AlSi10Mg 3-parameter Weibull distribution of (a) yield strength, (b) ultimate tensile strength, (c) Young's modulus, (d) elongation

number of samples N, Anderson-Darling statistic, and the p-value for each rack. The majority of the mechanical properties listed in the table have poor goodness-of-fit (AD) statistics and p-values that reject the null hypothesis. In other words, the threshold values do not represent statistically accurate extreme values. Furthermore, many of the mechanical properties of the AlSi10Mg alloy in this study fail to meet the minimum parameters set forth in the ASTM standard for this material in the SR1 condition **[72]**. The required acceptable values are 241 MPa for ultimate strength, 138 MPa yield strength, and 10% ductility for the heat treatment used in this study. Fractography of the tensile specimens reveal a significant amount of porosity caused by incorrect processing parameters and are determined to be the source of inadequacy in mechanical properties. The following section will discuss this in further detail.

	Sample	Shape	Scale	Thresh	N	AD	P
Yield Stress (MPa)	Build 1 - R1	3.067	13.81	138.2	26	0.268	>0.500
	Build 1 - R2	1.934	9.642	147.5	34	0.18	>0.500
	Build 2 - R1	6.29	37.96	124.4	35	0.311	0.479
	Build 2 - R2	2.374	15.66	144.2	35	0.512	0.183
Tensile Strength (MPa)	Build 1 - R1	3.068	20.35	202.9	33	0.516	0.148
	Build 1 - R2	6.608	42.27	180.3	35	0.253	>0.500
	Build 2 - R1	9.536	83.58	148.7	38	0.215	>0.500
	Build 2 - R2	2.897	28.04	201.5	36	0.315	>0.500
Modulus (GPa)	Build 1 - R1	2.435	5.743	42.11	31	0.315	>0.500
	Build 1 - R2	4.069	8.813	39.17	35	0.462	0.196
	Build 2 - R1	3.782	9.392	40.69	35	0.298	>0.500
	Build 2 - R2	2.609	7.037	42.23	35	0.357	0.432
Elongation (%)	Build 1 - R1	5.688	4.98	0.9204	33	0.342	0.41
	Build 1 - R2	3.015	2.324	3.004	35	0.513	0.152
	Build 2 - R1	4.943	4.879	0.4958	38	0.572	0.089
	Build 2 - R2	2.393	2.612	2.663	36	0.534	0.154

Table 14: AlSi10Mg Weibull parameters

Section 4.3: AlSi10Mg Fractography

Controlling porosity with the use of process parameter optimization is a major topic in the additive manufacturing community **[8, 14, 17, 25, 58]**. The process parameters used for this material were not available, however, it is hypothesized that the settings used are the leading cause of porosity present in the samples. While laser power, layer thickness, and scanning speed play key roles in part quality and density, hatch spacing, and scanning strategy have proven to be determining factors in sample porosity **[17]**. The observed porosity in the material covered in this chapter is hypothesized to have formed due to the scanning strategy used during fabrication. As mentioned in the first section of this chapter, the lack of fusion defects are identified as the leading form of porosity present in the material being studied. These types of defects contribute to inferior performance as they act as stress concentration sites and reduce the effective load-bearing cross-sectional area. Figure 25 shows images taken using a Keyence VHX 5000 microscope of a tensile bar from each rack, revealing a lack of fusion porosity present in every sample. Circled in red are locations where voids are open to the surface and spray paint was able to penetrate during speckling. These surface openings may be due to an accumulation of gas escaping the build volume, as it has been shown that hydrogen gas is prominent in SLM AlSi10Mg **[73]**. They may also be due to incorrect contour pass settings, as there is an obvious gap between the outer edge and fill passes. Future work is needed to explore the validity of this hypothesis. The lack-of-fusion voids are consistent in size, shape, and location for all ~140 samples tested, providing evidence that they are due to a process parameter error. Each sample on the tensile rack failed at various locations along the build direction, so it is assumed that the large tunnel voids

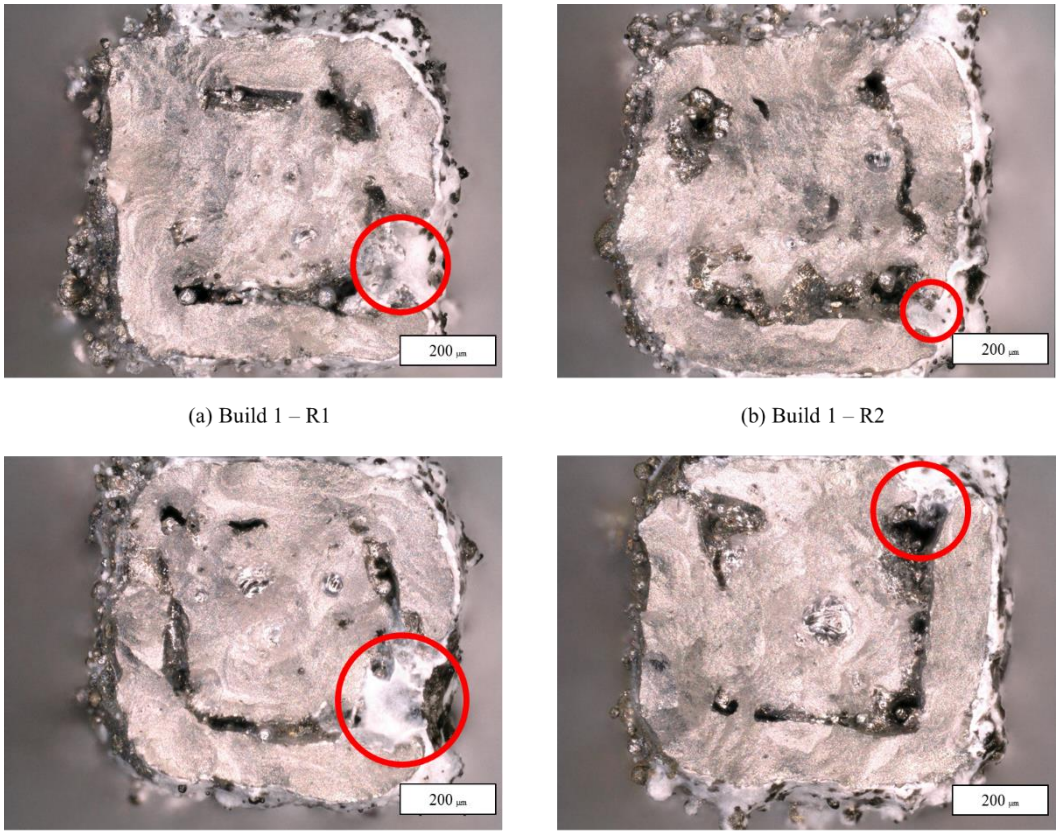

(a) Build 1 – R1 (b) Build 1 – R2

(c) Build 2 – R1 (d) Build 2 – R2

Figure 25: Fractography of AlSi10Mg showing lack of fusion voids and surface openings on samples (a) Build 1-R1, (b) Build 1-R2, (c) Build 2-R1, (d) Build 2-R2

that follow the edge contour are present throughout the entire sample. The fused perimeter around the porous tunnels measured about 120 microns wide, on average, suggesting that the observed porosity may be linked to perimeter scans of the material during printing. Fractography of the vertically-printed Charpy specimens that accompanied the tensile bars for testing also revealed signs of lack of fusion porosity around the entire edge of the samples, consistently around 120 microns in width. Figure 26 shows an SEM image of one edge of an AlSi10Mg charpy bar, (a), with a close-up detailing the lack of fusion tunnel and width of the fused contour pass, (b). The exact process settings are not currently known, however, based on the consistency of the

porous tunnel location, it is postulated that perimeter contour scans and hatch spacing are the sources of the lack of fusion porosity.

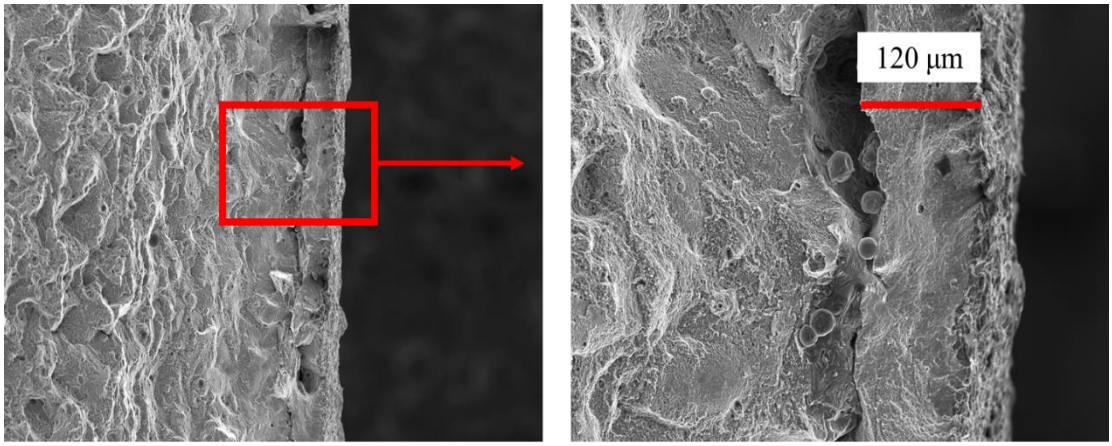

Figure 26: SEM Images of a charpy bar fracture surface (a) and a zoomed in portion showing lack of fusion porosity near the edge (b)

While the fused zone between the edge of the samples and the edge of the porous tunnel are consistent, the size of the porous tunnels are not. The variability in mechanical properties shown in Figure 23, as well as statistically represented in Table 14, can be attributed to the amount of variation in porosity between samples. An increase in voids decreases the effective load-bearing area, as mentioned in the IN625 chapter, and a decrease in effective area negatively affects the mechanical properties. A quantitative analysis was conducted, using a poor performing sample and an excellent performing sample, and showed that the effect of voids on the load-bearing area greatly influenced mechanical performance. ImageJ, an open source image processing program developed by the National Institute of Health, was used to alter the brightness and contrast of fracture surface images and outline edges of the voids. A pixel-to-mm scale was calibrated for the microscope and measurements of the effective area were made. Figure

27 shows the highlighted edges used for the measurement of a poor performing sample, (a), and an optimally performing samples, (b). The effective area measurements are normalized by gross area measurements, assessed at the outer edges of the samples, and verified by the area measurements provided by AVID. The poorly-performing sample had an effective area of about 60%, whereas the excellent-performing specimen was calculated at 74%. Both samples had similar modulus and yield strength values, 50 GPa and 166 MPa, respectively, however, the ultimate tensile strength and elongation at failure varied significantly. The strength and ductility values are given as 220 MPa and 2.8% for the poorly performing specimen shown in Figure 27 (a), respectively, with the better performing sample having a strength of 247 MPa and failing at 8.1% elongation, presented in Figure 27 (b). The stronger sample reached ultimate strength at 5.5% strain, nearly twice the amount of elongation obtained by the weaker sample, confirming that the increased presence of voids triggers premature failure. Correcting modulus, yield strength, and ultimate tensile strength for the effective area significantly increases the values. Assuming an average effective area of 67%, the corrected mean values become 64 GPa for modulus, 208 MPa for yield stress, and 298 MPa for ultimate tensile strength.

Hardness indentations made using the acceptance testing procedure may have been affected by the observed porous tunnels. As the indentations are made, the tunnels may have collapsed under pressure and produced lower hardness values. The location of the pores are consistent throughout the components, potentially explaining the minimal variation between the low values. To test this hypothesis, a sample was polished below the depth of the voids and hardness indentations made on the sample showed comparable

results with those reported in Section 4.1. Based on these findings, it is likely that the pores had no effect on the hardness results.

While most of the mechanical properties for the better-performing sample exceeded the minimum requirements set forth in the ASTM standard for this material, the elongation value still fell short of the 10% minimum elongation. The presence of voids in the material influence crack initiation and trigger premature plasticity, causing the material to fracture impetuously. The effects of these voids are exaggerated by the sub-size cross-sectional area of the tensile bars used in the study, as the effective load bearing area is already reduced by the surface roughness **[74]**. A surface roughness correction for area measurements would improve the overall strengths, however, these results are left out as this chapter was primarily focused on the role of internal voids since they are the dominant factor.

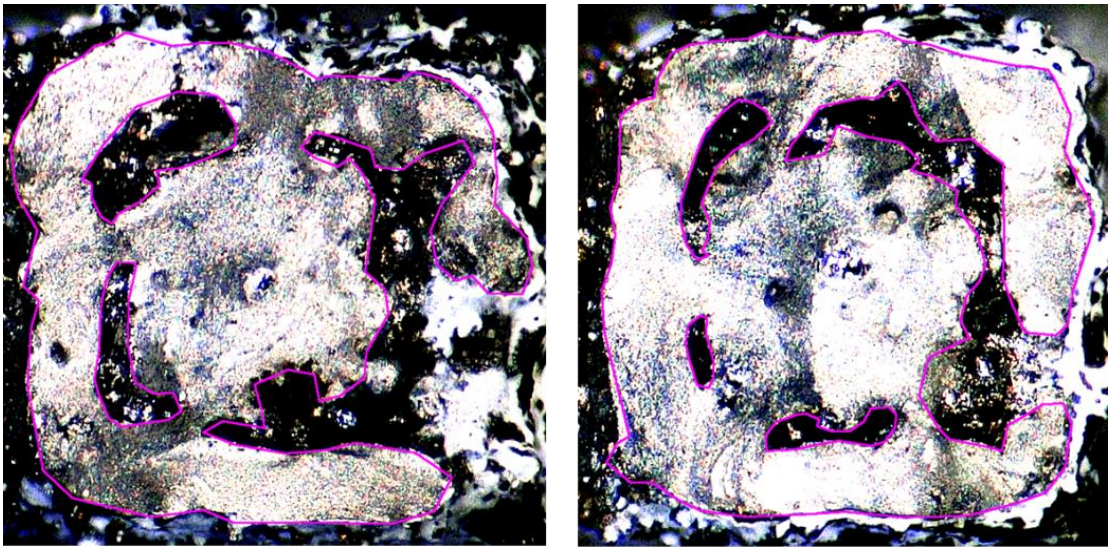

Figure 27: Effective area measurements of samples with (a) poor mechanical performance, (b) exceptional mechanical performance

Chapter 5 – Summary

This thesis presented a unique method for stochastically determining mechanical properties of two commonly used additively manufactured alloys, both fabricated by the LPBF process. The high-throughput testing method, derived from Boyce and Salzbrenner **[13, 20]** and modified to reduce the need for operator intervention, allowing for rapid characterization of sub-size tensile bar mechanical performance. Cameras normal to the front and side faces of the tensile bars enabled the use of non-contact digital strain evaluation and cross-sectional area calculation. When coupled with the AVID and BATS MatLab software packages, the testing and raw results of ~400 tensile bars could be processed in a day's work.

The high-throughput testing procedure was applied to determine the stochastic behavior of various heat-treated Inconel 625 specimens, specifically in the stress relieved, solutioned, and hot isostatic pressed conditions, as well as the effect of recycling the powder. The relatively large number of samples tested allowed for a statistical analysis of the average behavior in addition to the low-probability extreme values, an important parameter in component design.

An acceptance testing procedure is also presented in this study as a method to verify build parameters with minimal space utilized on the build tray. Measuring density, hardness, and impact toughness provide a superficial but informative overview of anticipated characteristics of the build, especially when correlated to properties of other builds composed of similar processing parameters and material. The application of the acceptance testing procedure, combined with the results of high-throughput testing,

reveals the AlSi10Mg alloy had consistently low strength and ductility values compared to typical properties for this material.

Inconel 625

The microstructure and mechanical properties of IN625 were characterized in this study. The stress relieved samples, in both the virgin and once-reused powder conditions, had nominally identical mechanical properties. Microstructural analysis of the two powder conditions showed coherent results, with some texture in the <001> orientation. The columnar grain growth observed in the EBSD images suggests anisotropy played a role in decreased elasticity compared to the solution annealed and hot isostatic pressed samples, as nickel has a strong anisotropic ratio.

The solution and hot isostatic press heat treatments following stress relief resulted in recrystallization and coarsening of the grains. Annealing twins are observed in both sample sets due to low stacking-fault free energy, producing higher grain boundary misorientation than the stress relieved samples. An increase in work hardening of the solution treated and HIP samples are attributed to the low SFE, as both materials had significantly lower yield stress but commensurate ultimate tensile strength with the stress relieved samples. An increase in grain size associated with the additional heat treatment is the reason for the decreased yield strength, as explained by the Hall-Petch relation. EBSD of the solution heat treated sample exhibited a <101> texture with other orientations along the lower portion of the IPF, while the HIP sample expressed a <111> orientation. The difference in orientation is likely due to local inhomogeneities as the modulus values of both materials closely resembled one another, suggesting a similar

texture. Future studies are needed to examine grain orientation on a larger scale to determine if the observed properties are local irregularities or consistent throughout the material.

The ductility of the HIPed material was found to be consistently low relative to the other heat treatments. The testing of hundreds of samples in this study revealed the inconsistency is attributed to material properties and not an isolated event. Density measurements were conducted to determine if porosity contributed to the abnormal elongation results. Based on the findings, the HIPed material displayed the lowest density, however, it is unlikely porosity facilitated premature failure as the calculated values of all specimens were within 0.2% of each other. CT images of a HIPed sample exhibit a small number of cracks on the surface, likely facilitating pockets of air during measurements and slightly reducing relative density calculations. Further investigation of the irregular ductility involved EDS analysis as previous studies of IN625 has shown the presence of precipitates negatively affecting elongation. Nb-rich carbides are observed in the Sol HT and HIP specimens, however, significantly more were identified in the HIPed material with an obvious increase in size. The intergranular Nb-rich carbides initiate plastic deformation and are presented as the cause of premature failure.

The ~400 specimens tested provided sufficient data for statistical analysis. The mechanical properties exhibited limited variation within and between racks of tensile bars, providing a range of properties for each heat treatment. 3-parameter Weibull distributions of the yield strength, ultimate strength, modulus, and ductility indicated low-probability extreme values above the minimum requirements set by ASTM standards. Although meeting or exceeding the lower threshold parameters, the sub-size tensile bars

demonstrated reduced strengths when compared to standard size components presented in other studies. Correcting for surface roughness tightened the gap between strengths of the two sizes, however, other factors such as stress concentration at voids likely influence stresses within the sub-size tensile bars. More high-throughput testing, with a large sample population and surface roughness values representative of the applications in which they will be used, is necessary to develop specifications for additively manufactured material properties for design.

AlSi10Mg

The density, hardness, and impact toughness values assessed as part of the acceptance testing procedure of the stress relieved AlSi10Mg were indicative of the mechanical properties exhibited during high-throughput testing. Connected internal lack of fusion porosity, consistently located around the perimeter of the samples, is observed via post-test fractography. The interconnected voids were a consequence of incorrect processing parameters and resulted in a less dense material, confirmed by the findings in this study. A linear relation between impact toughness and density indicated this type of analysis provides valuable insight into the role of porosity on mechanical properties.

The lack of fusion acted as a catalyst for premature failure at strengths significantly lower than the minimum parameters established in the ASTM standard. The variability of mechanical properties is attributed to the extent of porosity present within the samples. Estimations of effective load-bearing area revealed the combination of voids and surface roughness negatively impacted the measurements by as much as 40% in the worst-case scenario, and at best by 25%. The lead performance of all AlSi10Mg samples

tested complied with strength specifications, however, ductility failed prematurely. Effective area corrections increased the strength values well above the minimum ASTM values. The lack of fusion voids initiated crack formation due to concentrations in stress and are the root cause of inadequate mechanical performance.

Future Considerations

The hi-throughput tensile testing procedure provides immense amounts of data, however, current analysis methods such as microstructure evaluation and computed tomography scans are limited in terms of rapid assessment. Opportunities exist to optimize these procedures. The high-throughput method introduces variation to other published mechanical properties, demonstrated to be dependent on the size of the material used. Future innovations to the process could address the scaling factor. The acceptance testing approach to component verification could further benefit from automation as the process is laborious and time-intensive.

The abnormal results observed in the characterization of Inconel 625 mechanical properties opens the door for further investigations and topics of research. One such topic is the precipitate formation and densification of LPBF Inconel 625 during the HIP process. The amount of research on this topic is minimal, providing grounds for a better understanding of the impact of HIP heat treatment on microstructure and precipitate kinetics. The reused powder in this study was only subjected to a stress relief heat treatment due to a limited time scale. The impact on mechanical performance was negligible, so characterization of the other heat treatment effects on reused powder would be beneficial.

Appendix

Element	S_{11} (10^{-2} GPa^{-1})	S_{12} (10^{-2} GPa^{-1})	S_{44} (10^{-2} GPa^{-1})
Nickel	0.734	-0.274	0.802
Chromium	0.358	-0.075	0.867
Molybdenum	0.280	-0.078	0.910
Niobium	0.690	-0.249	3.420

Table 15: Elastic Compliances for Monocrystalline Metals, [38]

Element	C_{11} (GPa)	C_{12} (GPa)	C_{44} (GPa)
Nickel	246.5	147.3	124.7

Table 16: Elastic Stiffness of Monocrystals, [38]

	I_{i1}	I_{j2}	I_{k3}	$(I_{i1}^2 I_{j2}^2 + I_{j2}^2 I_{k3}^2 + I_{i1}^2 I_{k3}^2)$
[100]	1	0	0	0
[110]	$\sqrt{2}/2$	$\sqrt{2}/2$	0	$1/4$
[111]	$1/\sqrt{3}$	$1/\sqrt{3}$	$1/\sqrt{3}$	$1/3$

Table 17: Direction Cosines

References

1. Isaza, J. and P. Aumund-Kopp, *Additive Manufacturing With Metal Powders: Design for Manufacture Evolves Into Design for Function.* Powder Metall Rev, 2014. **3**(2): p. 41-50.
2. Kruth, J.P., M.C. Leu, and T. Nakagawa, *Progress in Additive Manufacturing and Rapid Prototyping.* CIRP Annals - Manufacturing Technology, 1998. **47**(2): p. 525-540.
3. Hedges, M. and N. Calder, *Near net shape rapid manufacture & repair by LENS, in: Cost. Eff. Manuf. via Net-Shape Process.* Meet. Proc. RTO-MP-AVT-139, 2006. **2**: p. 13.
4. Wohlers, T., *Wohlers Report 2016.* Wohlers Associates, Inc., 2016.
5. K. Vartanian, T.M., *Accelerating industrial adoption of metal additive manufacturing technology.* JOM, 2016. **68**(3): p. 806-810.
6. Gibson, I., D. Rosen, and B. Stucker, *Additive Manufacturing Technologies*. 2015.
7. Li, C., et al., *Microstructure evolution characteristics of Inconel 625 alloy from selective laser melting to heat treatment.* Materials Science and Engineering: A, 2017. **705**: p. 20-31.
8. Kempen, K., et al., *Mechanical Properties of AlSi10Mg Produced by Selective Laser Melting.* Physics Procedia, 2012. **39**: p. 439-446.
9. Finfrock, C.B., et al., *Effect of Hot Isostatic Pressing and Powder Feedstock on Porosity, Microstructure, and Mechanical Properties of Selective Laser Melted AlSi10Mg.* Metallography, Microstructure, and Analysis, 2018. **7**(4): p. 443-456.
10. Lass, E.A., et al., *Formation of the Ni3Nb δ-Phase in Stress-Relieved Inconel 625 Produced via Laser Powder-Bed Fusion Additive Manufacturing.* Metallurgical and Materials Transactions A, 2017. **48**(11): p. 5547-5558.
11. Strano, G., et al., *Surface roughness analysis, modelling and prediction in selective laser melting.* Journal of Materials Processing Technology, 2013. **213**(4): p. 589-597.
12. Yadroitsev, I. and I. Smurov, *Surface Morphology in Selective Laser Melting of Metal Powders.* Physics Procedia, 2011. **12**: p. 264-270.
13. Salzbrenner, B.C., et al., *High-throughput stochastic tensile performance of additively manufactured stainless steel.* Journal of Materials Processing Technology, 2017. **241**: p. 1-12.
14. Grasso, M. and B.M. Colosimo, *Process defects andin situmonitoring methods in metal powder bed fusion: a review.* Measurement Science and Technology, 2017. **28**(4).
15. Amato, K., *Comparison of Microstructures and Properties for a Ni-Base Superalloy (Alloy 625) Fabricated by Electron Beam Melting.* Journal of Materials Science Research, 2012. **1**(2).
16. Keller, T., et al., *Application of Finite Element, Phase-field, and CALPHAD-based Methods to Additive Manufacturing of Ni-based Superalloys.* Acta Mater, 2017. **139**: p. 244-253.

17. Aboulkhair, N.T., et al., *Reducing porosity in AlSi10Mg parts processed by selective laser melting.* Additive Manufacturing, 2014. **1-4**: p. 77-86.
18. Deibler, L., et al. *Effects of AlSi10Mg feedstock condition on part properties*. in *Annual International Solid Freeform Fabrication Symposium*. 2017. Austin, TX.
19. King, W.E., et al., *Observation of keyhole mode laser melting in lasder powder-bed fusion additive manufacturing.* Material Process Technology, 2014. **214**: p. 2195-2925.
20. Boyce, B.L., et al., *Extreme-Value Statistics Reveal Rare Failure-Critical Defects in Additive Manufacturing.* Advanced Engineering Materials, 2017. **19**(8).
21. ASTM, *Standard Test Methods for Tension Testing of Metallic Materials.* American Society for Testing and Materials, 2016. **E8**.
22. Gaynor, A.T., et al., *Topology Optimization for Additive Manufacturing: Considering Maximum Overhang Constraint*, in *15th AIAA/ISSMO Multidisciplinary Analysis and Optimization Conference*. 2014.
23. Solutions, C. *VIC Speckle Pattern Specifications*. 2019.
24. Bing Pan, H.X., Zhaoyang Wang, Kemao Qian, Zhiyong Wang, *Study on subset size selection in DIC speckle patterns.* Optics Express, 2008.
25. Jeon, T., et al., *Control of Porosity in Parts Produced by a Direct Laser Melting Process.* Applied Sciences, 2018. **8**(12).
26. ASTM, *Standard Test Methods for Rockwell Hardness of Metallic Materials.* ASTM International, 2015.
27. Hughes, S.E., *A Quick Guide to Welding and Weld Inspection*. 2009.
28. ASTM, *Standard Test Methods for Notched Bar Impact Testing of Metallic Materials.* ASTM International, 2013.
29. ASTM, *Standard Test Methods for Density of Compacted or Sintered Powder Metallurgy (PM) Products Using Archimedes' Principle.* ASTM B962-13, 2013: p. 1-7.
30. Leung, C.L.A., et al., *The effect of powder oxidation on defect formation in laser additive manufacturing.* Acta Materialia, 2019. **166**: p. 294-305.
31. ASTM, *Standard Specification for Additive Manufacturing Nickel Alloy (UNSN06625) with Powder Bed Fusion.* ASTM International, 2014.
32. Uhlmann, E., et al., *Additive Manufacturing of Titanium Alloy for Aircraft Components.* Procedia CIRP, 2015. **35**: p. 55-60.
33. L.C. Ardila, F.G., J.B. Gonzalez-Diaz, et al., *Effect of IN718 Recycled Powder Reuse on Properties of Parts Manufactured by Means of Selective Laser Melting.* Physics Procedia, 2014. **56**: p. 99-107.
34. Wright, S.I., M.M. Nowell, and D.P. Field, *A review of strain analysis using electron backscatter diffraction.* Microsc Microanal, 2011. **17**(3): p. 316-29.
35. Heating, I. *Engineering Concepts: Formation of Annealing Twins*. 2000; Available from: https://www.industrialheating.com/articles/86154-engineering-concepts-formation-of-annealing-twins?
36. Valerie Randle, H.D., Ian Cross, *Grain Boundary Misorientation.* Solid State and Materials Science, 2001. **5**: p. 3-8.
37. Kreitcberg, A., V. Brailovski, and S. Turenne, *Effect of heat treatment and hot isostatic pressing on the microstructure and mechanical properties of Inconel 625*

alloy processed by laser powder bed fusion. Materials Science and Engineering: A, 2017. **689**: p. 1-10.
38. Meyers, M.A. and K.K. Chawla, *Mechanical Behvior of Materials*. 2009: Cambridge Univserity Press.
39. Metals, S. *Inconel Alloy 625*.
40. Zhang, K., et al., *Effect of Hot-Isostatic-Pressing Parameters on the Microstructure and Properties of Powder Ti-6Al-4V Hot-Isostatically-Pressed Samples.* Metallurgical and Materials Transactions A, 2010. **41**(4): p. 1033-1045.
41. Wang, M., et al., *A multi-scale study of Inconel 625 powders HIP process and construction of HIP maps.* The International Journal of Advanced Manufacturing Technology, 2016. **90**(9-12): p. 3055-3066.
42. Boyce, B.L., *A Sequential Tensile Method for Rapid Characterization of Extreme-value Behavior in Microfabricated Materials.* Experimental Mechanics, 2009. **50**(7): p. 993-997.
43. Luecke, W.E. and J.A. Slotwinski, *Mechanical Properties of Austenitic Stainless Steel Made by Additive Manufacturing.* J Res Natl Inst Stand Technol, 2014. **119**: p. 398-418.
44. ASTM, *Standard Practice for Size Scaling of Tensile Strengths Using Weibull Statistics for Advanced Ceramics.* ASTM C1683, 2019. **10**.
45. Han, Z., et al., *A three-parameter Weibull statistical analysis of the strength variation of bulk metallic glasses.* Scripta Materialia, 2009. **61**(9): p. 923-926.
46. Weibull, W., *A Statistical Distribution Function of Wide Applicability.* Journal of Applied Mechanics, 1951. **18**(3): p. 293-297.
47. Zahedi, H., et al., *The Effect of Fe-Rich Intermetallics on the Weibull Distribution of Tensile Properties in a Cast Al-5 Pct Si-3 Pct Cu-1 Pct Fe-0.3 Pct Mg Alloy.* Metallurgical and Materials Transactions A, 2007. **38**(3): p. 659-670.
48. Minitab. *Anderson-Darling Statistic*. 2018.
49. Marchese, G., et al., *Influence of heat treatments on microstructure evolution and mechanical properties of Inconel 625 processed by laser powder bed fusion.* Materials Science and Engineering: A, 2018. **729**: p. 64-75.
50. Hack, H., et al., *Mechanical properties of additive manufactured nickel alloy 625.* Additive Manufacturing, 2017. **14**: p. 105-115.
51. Sukumaran, A., R.K. Gupta, and V. Anil Kumar, *Effect of Heat Treatment Parameters on the Microstructure and Properties of Inconel-625 Superalloy.* Journal of Materials Engineering and Performance, 2017. **26**(7): p. 3048-3057.
52. R.P. Martukanitz, E.W.R., M. Brennan, D.J. Corbin, P. Coutts, G. Jones, K.C. Meinert Jr., W.F. Mitchell, E. West *Development of Additive Manufacturing Technology to Reduce Implementation Risk.* Technical Memorandum File No. 19-007, 2019. **Applied Research Laboratory, Pennsylvania State University**.
53. Frazier, W.E., *Metal Additive Manufacturing: A Review.* Journal of Materials Engineering and Performance, 2014. **23**(6): p. 1917-1928.
54. Peeyush Nandwana, W.H.P., Ryan R. Dehoff, Larry E. Lowe, *Recyclability Study on Inconel 718 and Ti-6Al-4V Powders for Use in Electron Beam Melting.* Metallurgical and Materials Transactions B, 2015. **47B**: p. 754-762.

55. Tang, H.P., et al., *Effect of Powder Reuse Times on Additive Manufacturing of Ti-6Al-4V by Selective Electron Beam Melting.* Jom, 2015. **67**(3): p. 555-563.
56. Hansen, N., *Hall–Petch relation and boundary strengthening.* Scripta Materialia, 2004. **51**(8): p. 801-806.
57. Gao, Y. and M. Zhou, *Superior Mechanical Behavior and Fretting Wear Resistance of 3D-Printed Inconel 625 Superalloy.* Applied Sciences, 2018. **8**(12).
58. Kok, Y., et al., *Anisotropy and heterogeneity of microstructure and mechanical properties in metal additive manufacturing: A critical review.* Materials & Design, 2018. **139**: p. 565-586.
59. Wang, P., et al. *Anisotropic Mechanical Properties in a Big-Sized Ti-6Al-4V Plate Fabricated by Electron Beam Melting*. 2016. Cham: Springer International Publishing.
60. Cain, V., et al., *Crack propagation and fracture toughness of Ti6Al4V alloy produced by selective laser melting.* Additive Manufacturing, 2015. **5**: p. 68-76.
61. Lethbridge, Z.A.D., et al., *Elastic anisotropy and extreme Poisson's ratios in single crystals.* Acta Materialia, 2010. **58**(19): p. 6444-6451.
62. Hasebe, T., M. Sakane, and M. Ohnami, *Elastic Anisotropy of Directionally Solidified Superalloy.* Engineering Materials and Technology, 1992. **114**: p. 141-146.
63. Chlebus, E., et al., *Effect of heat treatment on the microstructure and mechanical properties of Inconel 718 processed by selective laser melting.* Materials Science and Engineering: A, 2015. **639**: p. 647-655.
64. Rao, G.A., et al., *Effect of standard heat treatment on the microstructure and mechanical properties of hot isostatically pressed superalloy inconel 718.* Materials Science and Engineering: A, 2003. **355**(1-2): p. 114-125.
65. Zhang, J., et al., *Characterization of the prior particle boundaries in a powder metallurgy Ti2AlNb alloy.* Journal of Materials Science & Technology, 2019. **35**(11): p. 2513-2525.
66. Rao, G.A., M. Srinivas, and D.S. Sarma, *Influence of modified processing on structure and properties of hot isostatically pressed superalloy Inconel 718.* Materials Science and Engineering: A, 2006. **418**(1-2): p. 282-291.
67. Rosalie, J.M., et al., *Effect of precipitation on strength and ductility in a Mg–Zn–Y alloy.* Journal of Alloys and Compounds, 2013. **550**: p. 114-123.
68. Gussev, M.N., et al., *Sub-size tensile specimen design for in-reactor irradiation and post-irradiation testing.* Nuclear Engineering and Design, 2017. **320**: p. 298-308.
69. Kumar, K., et al., *Optimisation of thickness of miniature tensile specimens for evaluation of mechanical properties.* Materials Science and Engineering: A, 2016. **675**: p. 32-43.
70. Shin, C., et al., *Specimen size effects on the weakening of a bulk metastable austenitic alloy.* Materials Science and Engineering: A, 2015. **622**: p. 67-75.
71. Thijs, L., et al., *Fine-structured aluminium products with controllable texture by selective laser melting of pre-alloyed AlSi10Mg powder.* Acta Materialia, 2013. **61**(5): p. 1809-1819.

72. ASTM, *Standard for Additive Manufacturing - Finished Part Properties - Specification for AlSi10Mg with Powder Bed Fusion - Laser Beam.* ASTM International, 2018.
73. Harvey, J.-P. and P. Chartrand, *Modeling the Hydrogen Solubility in Liquid Aluminum Alloys.* Metallurgical and Materials Transactions B, 2010. **41**(4): p. 908-924.
74. Susan, D.F., T.B. Crenshaw, and J.S. Gearhart, *The Effects of Casting Porosity on the Tensile Behavior of Investment Cast 17-4PH Stainless Steel.* Journal of Materials Engineering and Performance, 2015. **24**(8): p. 2917-2924.